Role of Catalyst Support and Regioselectivity of Molecular Adsorption on a Metal Oxide Surface: NO Reduction on Cu/γ-Alumina

Wataru Ota,[†,‡] Yasuro Kojima,[‡] Saburo Hosokawa,[‡,¶] Kentaro Teramura,[‡,¶] Tsunehiro Tanaka,[‡,¶] and Tohru Sato*,[†,‡,¶]

†*Fukui Institute for Fundamental Chemistry, Kyoto University, Sakyo-ku, Kyoto 606-8103, Japan*

‡*Department of Molecular Engineering, Graduate School of Engineering, Kyoto University, Nishikyo-ku, Kyoto 615-8510, Japan*

¶ *Elements Strategy Initiative for Catalysts & Batteries (ESICB), Kyoto University, Kyotodaigaku Katsura, Nishikyo-ku, Kyoto 615-8245, Japan*

E-mail: tsato@scl.kyoto-u.ac.jp

Abstract

The role of catalyst support and regioselectivity of molecular adsorption on a metal oxide surface is investigated for the NO reduction on a Cu/γ-alumina heterogeneous catalyst. For the solid surface, computational models of the γ-alumina surface are constructed based on the Step-by-Step Hydrogen Termination (SSHT) approach. Dangling bonds, which appear by cutting the crystal structure of a model, are terminated stepwise with H atoms until the model has an appropriate energy gap. The obtained SSHT models exhibit the realistic infrared (IR) and ultraviolet-visible (UV/Vis) spectra. Vibronic coupling density (VCD), as a reactivity index, is employed to elucidate

the regioselectivity of the Cu adsorption on the γ-alumina and that of the NO adsorption on the Cu/γ-alumina in place of the frontier orbital theory that could not provide clear results. We discovered that the highly dispersed Cu atoms are loaded on Lewis-basic O atoms, which is known as *anchoring effect*, located in the tetrahedral sites of the γ-alumina surface. The role of the γ-alumina support is to raise the frontier orbital of the Cu catalyst, which in turn gives rise to the electron back-donation from the Cu/γ-alumina to NO. In addition, the penetration of the VCD distribution of the Cu/γ-alumina into the γ-alumina support indicates that the excessive reaction energies dissipate into the support after the NO adsorption and reduction. In other words, the support plays the role of a heat bath. The NO reduction on the Cu/γ-alumina proceeds even in an oxidative atmosphere because the Cu–NO bond is strongly bounded compared to the Cu–O_2 bond.

Keywords

γ-alumina, NO reduction, anchoring effect, regioselectivity, vibronic couplings

Introduction

Three-way catalysts are used in automobiles to remove nitrogen oxides, carbon monoxide, and hydrocarbons from exhaust gas. Typical components of the three-way catalysts are platinum-group metal (PGM) species such as Rh, Pd, and Pt. In particular, Rh is responsible for reducing nitrogen oxides to N_2.[1,2] Thus, the NO adsorption on the Rh surface has been extensively studied.[3] In addition to the experiments, theoretical calculations have also attempted to reveal the NO reduction processes on the Rh catalysts.[4–6] Nevertheless, the reduction mechanism, especially the role of the catalyst support, remains unknown. For example, Ward *et al.* investigated the electronic states of $(NO)_2$ on the Rh, Pd, and Pt surfaces using the extended Hückel theory.[7] Electron back-donation occurs from the Rh d

2

bands to the $(NO)_2$ 2π orbital because the d bands are energetically close to the 2π orbital. The 2π orbital has a bonding character in the N–N bond and anti-bonding character in the N–O bonds. Consequently, the N–N bond is strengthened while the N–O bonds are weakened owing to back-donation, which is suitable for the reduction of NO to N_2. In contrast to the Rh surface, the back-donation hardly occurs for the Pd and Pt surfaces because these d bands are energetically much lower than the $(NO)_2$ 2π orbital. Thus, the $(NO)_2$ adsorption on the catalysts can be important as an initial step of the NO reduction. Ward *et al.* also reported that the α-alumina support varies the Fermi level of the Rh, Pd, and Pt surfaces, which affects the strength of N–O bond on their surfaces.[8]

The replacement for Rh with a ubiquitous element such as Cu is desirable because Rh is an expensive and rare metal. Cu/γ-alumina is a heterogeneous catalyst that reduces nitrogen oxides with high efficiency.[9–13] The most important feature of Cu catalyst is that NO reduction proceeds in an oxidative atmosphere, whereas PGM catalyst hardly exhibits catalytic activity under such a condition. In other words, NO can be easily adsorbed on the Cu/γ-alumina even in the presence of O_2. The active site for the reduction is determined to be the highly dispersed Cu^{2+} species.[9] The degree of catalyst dispersion generally depends on the strength of the interaction between a catalyst and its support, which is known as an anchoring effect.[14,15] γ-alumina, one of transitional phases of the alumina, has been extensively used as a catalyst support.[16] Owing to the existence of various types of adsorption sites on its surfaces due to its amorphous structure, the adsorption sites of the Cu catalyst on the γ-alumina as well as those of the NO on the Cu/γ-alumina are not clear. Therefore, the regioselectivity of the adsorptions require clarification to investigate the mechanism of the NO reduction on the Cu/γ-alumina while considering the role of the catalyst support.

The identification of reactive sites on a molecule or solid surface is one of the important problems in quantum chemistry. The frontier orbital theory evaluates the stabilization arising from the charge-transfer interactions, and has been successful in clarifying the regioselectivity of chemical reactions.[17,18] However, this theory sometimes has difficulty in

predicting reactive sites of a large system such as a solid surface due to the delocalization of frontier orbitals. This is because only the effect of the electronic states is considered. In addition to the stabilization via charge transfer interaction, further stabilization arises from structural relaxation caused by vibronic couplings. Vibronic coupling density (VCD), which is calculated from electronic and vibrational states, identifies reactive sites where the stabilization by vibronic couplings is significant in the course of a reaction.[19] The VCD analyses have successfully predicted the regioselectivity of the CO_2 and H_2 adsorption on the gallium oxide surface because of the localization of the vibrational states.[20,21] In addition, the VCD can be used as a reactivity index for the fullerenes[22–26] and aromatic hydrocarbons,[27] which are other examples where the frontier orbital theory fails to predict the regioselectivity. On the basis of the VCD analysis, the regioselectivity of the molecular adsorption has been predicted from the calculations of only the solid surface. In other words, there is no need to find an adsorption site with the minimum energy by calculating the energies of all possible molecular arrangements on a solid surface at the expense of computational costs.

For the VCD analysis for a solid surface, a computational model is required. Dangling bonds are generated on the metal oxide surfaces after simply cutting its three-dimensional (3D) crystal structure to obtain a slab or cluster model. Without any treatment of the dangling bonds, the computational model results in an open-shell electronic structure. Therefore, such models do not reflect the realistic electronic structure. We previously proposed a Step-by-Step Hydrogen Termination (SSHT) approach to circumvent this problem.[20] In this approach, H atoms are bonded step-by-step to O atoms with large orbital coefficient values or VCD distributions until the model exhibits an appropriate energy gap corresponding with experiments. Notably, in the models thus obtained, all the O atoms on the surface are not terminated with H atoms. Excess hydrogen termination may subsequently lead to excessive electron-doping, which would yield an unacceptably small energy gap.

In this study, we constructed SSHT slab and cluster models of the γ-alumina surface that reproduce the realistic electronic structures. The infrared (IR) and ultraviolet-visible

(UV/Vis) spectra were calculated to confirm the reliability of the models. Thereafter, based on these computational models, we investigated the regioselectivity of the Cu adsorption on the γ-alumina surface and that of the NO adsorption on the Cu/γ-alumina surface. The role of the catalyst support on the NO reduction was also discussed using the fragment orbital analysis[28] in which molecular orbitals of a system are decomposed into those of its fragments.

Theory

Vibronic Coupling Density (VCD)

Theory of VCD are reviewed in Refs. 29 and 30. Vibronic couplings are the interactions between nuclear vibrations and electrons. Within a crude adiabatic approximation, diagonal vibronic coupling constant (VCC) is defined by[31,32]

$$V_{+,\alpha} = \langle \Psi_+(\mathbf{r}; \mathbf{R}_0)|\mathcal{V}_\alpha|\Psi_+(\mathbf{r}; \mathbf{R}_0)\rangle, \tag{1}$$

where $|\Psi_+(\mathbf{r}; \mathbf{R}_0)\rangle$ is a charge-transfer state that depends on electronic coordinates, $\mathbf{r}$, at the equilibrium reference nuclear configuration $\mathbf{R}_0$. $\mathcal{V}_\alpha$ is the electronic part of a linear vibronic coupling operator given by

$$\mathcal{V}_\alpha = \left(\frac{\partial \hat{H}(\mathbf{r}, \mathbf{R})}{\partial Q_\alpha}\right)_{\mathbf{R}_0}, \tag{2}$$

where $\hat{H}(\mathbf{r}, \mathbf{R})$ denotes the molecular Hamiltonian, $\mathbf{R}$ the nuclear coordinates, and Q_α a mass-weighted normal coordinate of vibrational mode α. Using the Hellmann–Feynman theorem,[33,34] the diagonal VCC is expressed as follows:

$$V_{+,\alpha} = \left(\frac{\partial E_+(\mathbf{R}_0)}{\partial Q_\alpha}\right)_{\mathbf{R}_0}, \tag{3}$$

where $E_+(\mathbf{R}_0)$ are the eigenvalues of $|\Psi_+(\mathbf{r}; \mathbf{R}_0)\rangle$. The diagonal VCC can be evaluated from the gradient of a potential energy surface with respect to Q_α at $\mathbf{R}_0$.

Owing to the expression of $\mathcal{V}_\alpha$ as a sum of one-electron operators, $v_\alpha(\boldsymbol{x})$, the diagonal VCC is decomposed into the orbital contributions;[29,30] that is,

$$V_{+,\alpha} = \sum_{i \in \text{occ}} f_{i,\alpha}, \tag{4}$$

where $f_{i,\alpha}$ is the orbital vibronic coupling constant (OVCC) defined as follows:[29,30]

$$f_{i,\alpha} = \langle \psi_i(\boldsymbol{x})|v_\alpha(\boldsymbol{x})|\psi_i(\boldsymbol{x})\rangle. \tag{5}$$

Here, $|\psi_i(\boldsymbol{x})\rangle$ represents a one-electron state, or molecular orbital, whereas $\boldsymbol{x} = (x, y, z)$ the Cartesian coordinate of a single electron.

The diagonal VCD is given by the spatial distributions of the diagonal VCC as follows:

$$V_{+,\alpha} = \int \eta_{+,\alpha}(\boldsymbol{x})\, d\boldsymbol{x}. \tag{6}$$

$\eta_{+,\alpha}(\boldsymbol{x})$ as a function of $\boldsymbol{x}$ identifies a site where the VCC assumes a large value. $\eta_{+,\alpha}(\boldsymbol{x})$ is divided into the electronic and vibrational terms as follows:

$$\eta_{+,\alpha}(\boldsymbol{x}) = \Delta\rho(\boldsymbol{x}) \times v_\alpha(\boldsymbol{x}). \tag{7}$$

Here, $\Delta\rho(\boldsymbol{x})$ is the electron density difference between $|\Psi_+(\mathbf{r}; \mathbf{R}_0)\rangle$ and equilibrium reference state,

$$\Delta\rho(\boldsymbol{x}) = \rho_+(\boldsymbol{x}) - \rho_0(\boldsymbol{x}). \tag{8}$$

$v_\alpha(\boldsymbol{x})$ is the potential derivative given by

$$v_\alpha(\boldsymbol{x}) = \left(\frac{\partial u(\boldsymbol{x})}{\partial Q_\alpha}\right)_{\mathbf{R}_0}, \tag{9}$$

where $u(\boldsymbol{x})$ is an attractive electron-nucleus potential acting on a single electron. The VCD

analysis explores the origin of the VCC from the electronic and vibrational states.

Parr and Yang formulated the frontier orbital theory of chemical reactivity in terms of the conceptual density functional theory (DFT).[35,36] In their theory, the Fukui function is approximately equal to the frontier orbital density, and the highest occupied molecular orbital (HOMO) density is regarded as a reactivity index for electrophilic reactions, whereas the lowest unoccupied molecular orbital (LUMO) density is for nucleophilic reactions. Sato *et al.* previously demonstrated that the total differential of chemical potential, $d\mu$, can be expressed using the VCD, η_ξ, along a reaction mode, ξ;[19]

$$d\mu = 2\eta_N dN + \int \eta_\xi(\boldsymbol{x}) \ d\xi d\boldsymbol{x}, \tag{10}$$

where η_N denotes the absolute hardness, N the number of electrons, and $\eta_\xi(\boldsymbol{x})$ the VCD of reaction mode ξ. It is possible to conclude that the chemical reactions occur at a site where $\eta_\xi(\boldsymbol{x})$ is the largest because the chemical reactions are assumed to occur so as to maximize $d\mu$.[35,36] Therefore, $\eta_\xi(\boldsymbol{x})$ can be regarded as a reactivity index for chemical reactions including the effects of both the electronic and vibrational states on the regioselectivity. In the current study, the reaction mode was selected as an effective mode given by[22]

$$d\xi = \sum_\alpha \frac{V_{+,\alpha}}{\sqrt{\sum_\alpha |V_{+,\alpha}|^2}} dQ_\alpha, \tag{11}$$

which is the steepest descent direction of the structural relaxation after the charge transfer. $\eta_\xi(\boldsymbol{x})$ is represented as the product of $\Delta\rho(\boldsymbol{r})$ and potential derivative for the effective mode $v_\xi(\boldsymbol{x})$. The VCC with respect to the effective mode quantifies the stabilization via the structural relaxation following the charge transfer.

Fragment Orbital Analysis

Divide a molecule into fragments A and B. A molecular orbital, $\psi_m(\boldsymbol{x})$, is expanded in terms of those of fragments A, $\psi_k^A(\boldsymbol{x})$, and B, $\psi_l^B(\boldsymbol{x})$, which are known as *fragment orbitals*;[28,37]

$$\psi_m(\boldsymbol{x}) = \sum_k c_{km}^A \psi_k^A(\boldsymbol{x}) + \sum_l c_{lm}^B \psi_l^B(\boldsymbol{x}), \tag{12}$$

where k and l run over the molecular orbitals of A and B, respectively. The contribution of $\psi_k^A(\boldsymbol{x})$ to $\psi_m(\boldsymbol{x})$, P_{km}, is calculated from

$$P_{km} = |c_{km}|^2 + \sum_l c_{km}^A c_{lm}^B \langle \psi_k^A(\boldsymbol{x}) | \psi_l^B(\boldsymbol{x}) \rangle . \tag{13}$$

P_{km} represents the proportion of $\psi_k^A(\boldsymbol{x})$ in $\psi_m(\boldsymbol{x})$ because $\sum_k P_{km} + \sum_l P_{lm} = 1$.

Methods of Calculations

Figure 1 illustrates the computational procedure. γ-alumina is a metastable phase generated during a thermal transition from a Bohemito to α-alumina. Raybaud *et al.* constructed a 3D bulk model of the γ-alumina by following the transition process using molecular dynamics simulations.[38–40] Furthermore, they estimated that the (110), (100), and (111) surfaces respectively occupy 74, 16, and 10% of the total area of the γ-alumina surface,[39,40] which is consistent with experiments.[41] Therefore, we focused on the (110) surface because its surface area is dominant.

The slab model of the (110) surface was obtained by cutting the 3D bulk model.[38–40] The dangling bonds resulting from the homolytic cleavage of O atoms were treated using the SSHT approach. These dangling bonds should be terminated with H atoms because hydrations occur in the production of the γ-alumina.[42] In fact, the experimental IR spectra indicate the existence of OH groups on the γ-alumina surface.[43–46] A cluster model was also obtained by cutting the slab model. Compared with a slab model, a cluster model has the
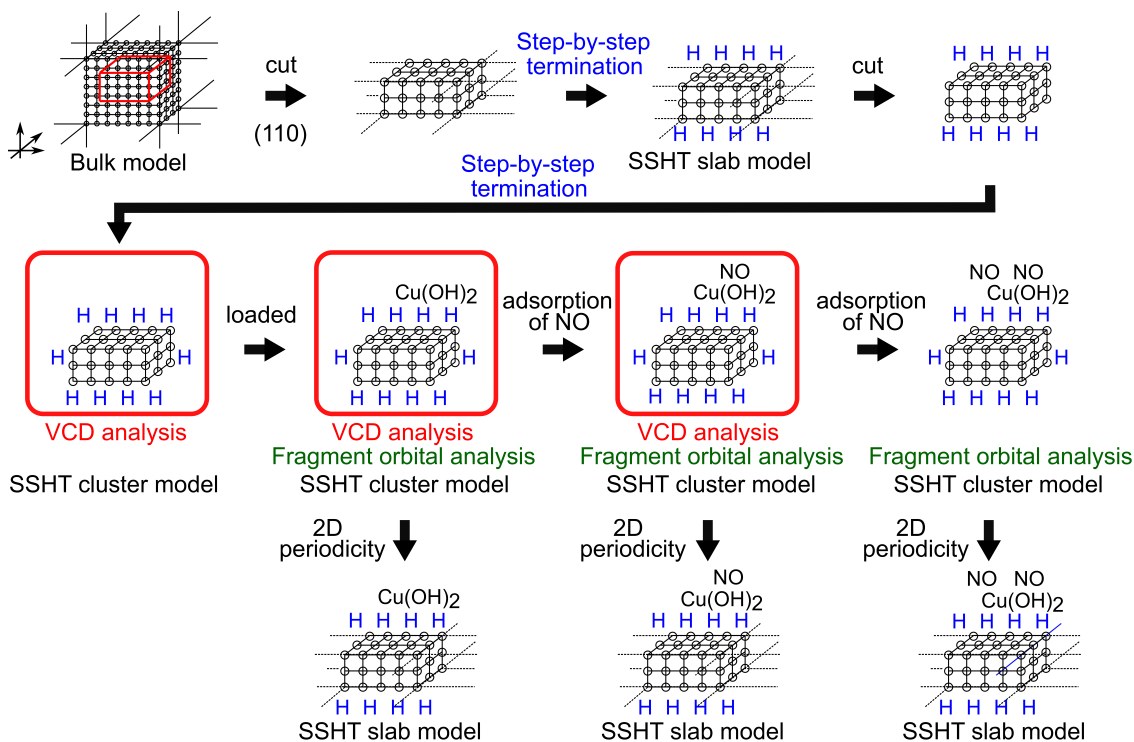
Figure 1: Schematic diagram of the computational procedure. The 3D bulk model is obtained from Refs. 38–40.

following advantages: (a) a single model contains multiple surfaces, (b) the computational cost is low because of the lack of $\mathbf{k}$ points in band calculations, and (c) the calculations of ionic states are possible. The dangling bonds generated when cutting the slab model were again treated using the SSHT approach.

The VCD analysis for the cluster model was performed to identify the Cu^{2+} adsorption site. $Cu(OH)_2$ is loaded on the γ-alumina surface because experiments indicate that a highly dispersed Cu^{2+} species has a coordination environment similar to $Cu(OH)_2$.[9] The adsorption sites of NO on the Cu/γ-alumina surface were also determined based on the VCD analyses for the cluster models. The adsorbed structures were obtained via geometry optimizations using the cluster and slab models. The optimizations were started from the structure in which adsorbents were placed on the sites where the VCD was localized. The fragment orbital analyses for the cluster models were performed to clarify the role of the γ-alumina support on the NO reduction.

The geometries of the neutral cluster models were optimized. The forces acting on the nuclei in the monocationic states at the neutral optimized structures were calculated to evaluate the VCC and VCD. The monocationic states were regarded as the charge-transfer states because the electron donations from the γ-alumina to Cu as well as that from the Cu/γ-alumina to NO were expected. The calculations of the cluster models were performed using Gaussian 09[47,48] at the B3LYP/3-21G level of theory. In the OVCC calculations, the restricted open-shell Kohn–Sham calculation was employed for simplicity. The IR spectrum was computed by summing the IR intensities broadened with the Gaussian function. The UV/Vis spectrum was computed by summing the oscillator strengths, which were evaluated by the time-dependent DFT theory, broadened with the Gaussian function. The fragment orbital analyses were performed based on the extended Hückel theory[49] with parameters provided in YAeHMOP.[50] The VCC, VCD, and fragment orbital analyses were performed using our in-house codes. The geometries of the slab models were also optimized. The calculations of the slab models were performed using Amsterdam Density Functional Band Structure Package[51,52] with the local density approximation and double zeta basis set.

Results and Discussion

Model Building of the γ-Alumina Surface.

Figure 2 illustrates a unit cell of the γ-alumina (110) surface slab obtained by cutting the three-dimensional bulk model.[38–40] The slab has a thickness of one unit cell layer in the z-direction. The lattice constants in the x- and y-directions are $a = 8.068$ and $b = 8.413$ Å, respectively. The unit cell has an inversion center. The γ-alumina consists of Al atoms coordinated by four or six O atoms, and the chemical formula of the unit cell is $Al_{16}O_{32}$.

Figure 3 presents the calculated band structure of the slab without hydrogen termination. The band gap of the γ-alumina surface was experimentally observed ranging from 2.5 to 8.7 eV.[53] However, the calculated band gap of the bare slab is zero because the Fermi
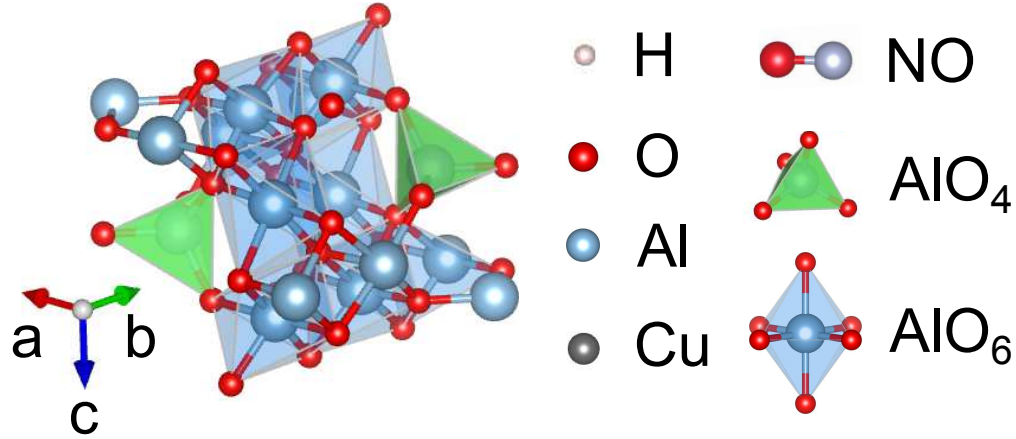
Figure 2: Unit cell of the γ-alumina (110) surface slab obtained by cutting the 3D bulk model in Refs. 38 and 40. The lattice constants are $a = 8.068$ and $b = 8.413$ Å. The unit cell has an inversion center. Hereafter, the atomic symbols in this figure are used without mentioning them.
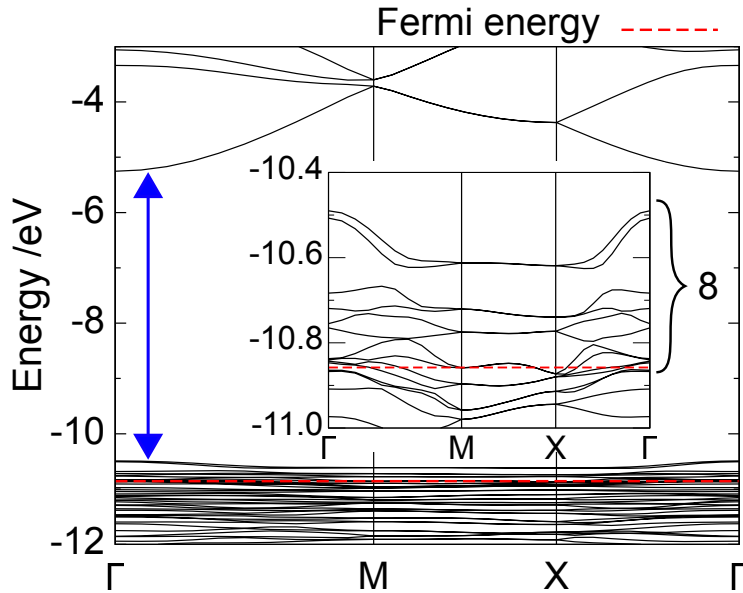

Figure 3: Calculated band structure of the γ-alumina slab without hydrogen termination. Sixteen H atoms should be bonded to the O atoms for the slab model to have an appropriate band gap indicated by a blue vertical arrow.

level intersects with the occupied bands. This discrepancy is attributed to the dangling bonds generated due to the homolytic cleavage of the O atoms when cutting the 3D crystal structure. The eight virtual bands should be occupied for the slab model to have an appropriate band gap corresponding with experiments. The hydrogen termination involves the electron-doping. Suppose that the formal charges of Al, O, and H are respectively 3+,

2−, and 1+, the net charge of the slab model becomes zero after introducing 16 H atoms because the chemical formula of the obtained unit cell becomes $Al_{16}O_{32}H_{16}$. In other words, the hydrogen termination results in the appropriate band gap and oxidation state.

(a)　　(b) LUCO (A, A')　　(c) LUCO+1 (E, E')

(d) LUCO+2 (L, L')　　(d) LUCO+3 (I, I')　　(e) LUCO+4 (H, H')

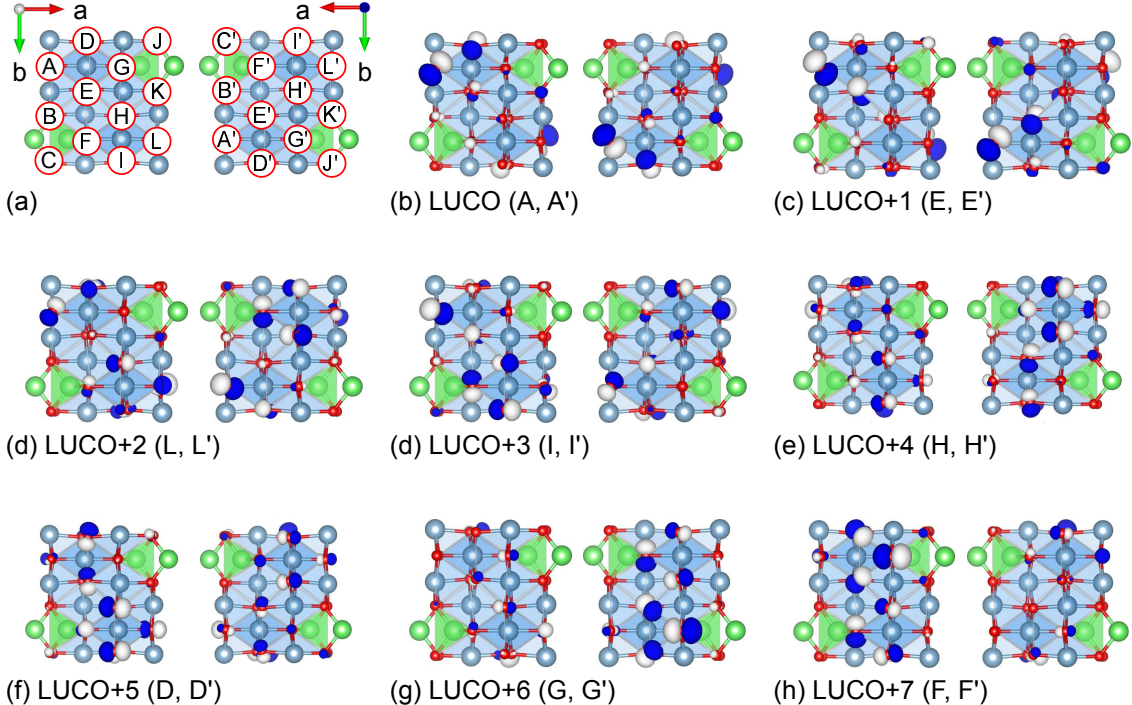(f) LUCO+5 (D, D')　　(g) LUCO+6 (G, G')　　(h) LUCO+7 (F, F')

Figure 4: (a) Labels of O atoms on the (110) surface, where the equivalent O atoms with respect to an inversion center are labeled using similar characters such as A and A'. (b)–(h) LUCO–LUCO+7 at the Γ-point of the bare slab. The O atoms that should be terminated with H atoms because of the large crystal orbital coefficients are provided in parentheses. Isosurface values are 5.0×10^{-2} a.u.

The sites for the hydrogen termination are determined based on the crystal orbital coefficients of the virtual bands at the Γ-point. Figure 4 (a) shows the O atoms on the front and reverse sides of the (110) surface where the equivalent O atoms with respect to an inversion center are labeled using similar characters such as A and A'. For each virtual band, two H atoms are bonded stepwise to the equivalent O atoms with large coefficients. Figure 4 (b)–(h) shows the unoccupied crystal orbitals at the Γ-point of the bare slab. The lowest unoccupied crystal orbital (LUCO) is mainly distributed on the O atoms at A and A'. Hence, two H atoms are bonded to these O atoms. The LUCO+1 is distributed at A, A', E, and E'. Since the O atoms at A and A' are already terminated, two H atoms are bonded to the

atoms at E and E'. In a similar manner, H atoms are bonded to the O atoms at L, I, H, D, G, and F based on the coefficients of the LUCO+2, +3, +4, +5, +6, and +7, respectively. Notably, the O atoms at the vertex of the tetrahedral Al species, i.e., B, C, J, and K, are not terminated because the coefficients of these O atoms are small. Figure 5 (a) illustrates the SSHT slab model after the geometry optimization of the model obtained above. This model has an appropriate wide band gap of 3.97 eV corresponding with experiments (Fig. S1). Cartesian coordinates of the SSHT slab model are tabulated in Table S1.
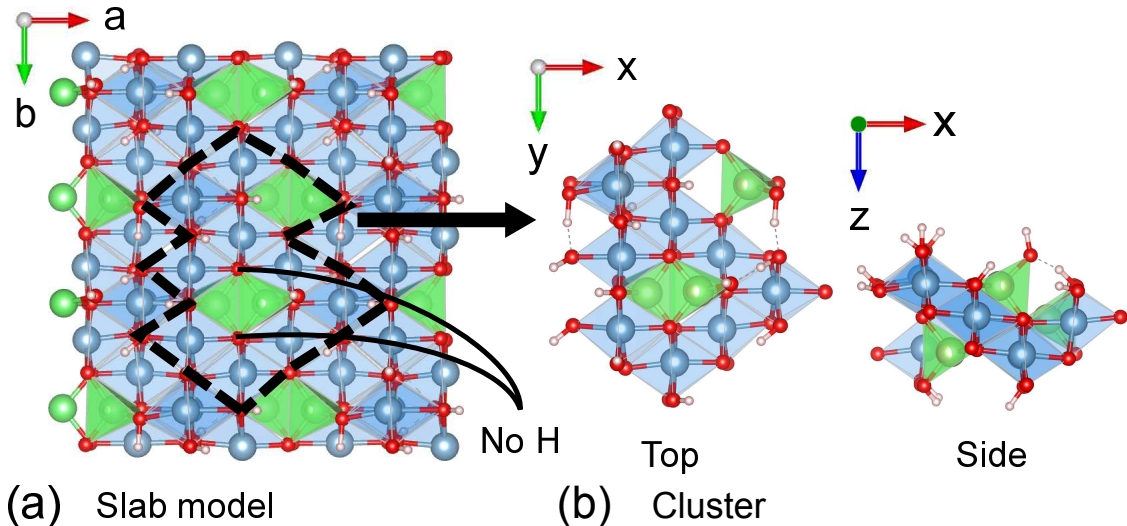

Figure 5: (a) SSHT slab model of the γ-alumina (110) surface after the geometry optimization. (b) Bare cluster obtained by cutting the slab model along with the dashed lines. The symmetry of the bare cluster is C_1.

A cluster model of the γ-alumina surface is obtained by cutting the SSHT slab model so that the O atoms without the hydrogen termination are centered (Fig. 5 (b)). The chemical formula of the bare cluster is $Al_{13}O_{40}H_{17}$. The symmetry is C_1. Figure 6 presents the orbital levels of the bare cluster. The energy gap of the bare cluster is calculated to be 0.58 eV, which is smaller than the experimental values of 2.5$\sim$8.7 eV.[53] This is because dangling bonds are generated when cutting the slab model. The twelve virtual orbitals are required to be fully occupied for the cluster model to have an appropriate energy gap corresponding with experiments. The addition of twenty-four H atoms results in the appropriate energy
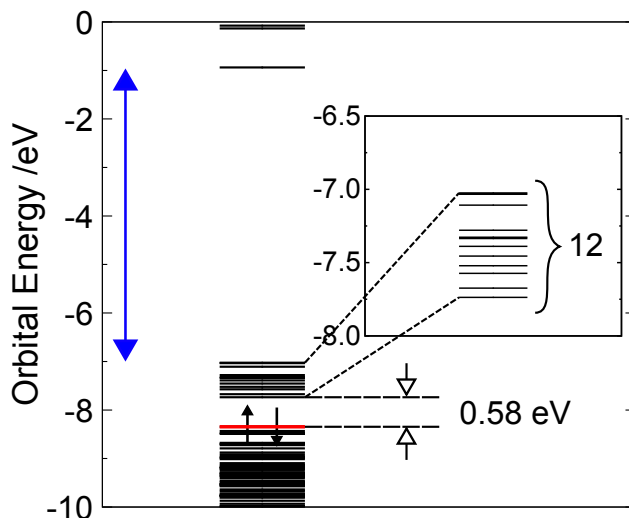
Figure 6: Calculated orbital levels of the bare cluster. Twenty-four H atoms should be bonded to O atoms for the cluster model to have an appropriate energy gap indicated by a blue vertical arrow.

gap as well as the oxidation state because the chemical formula of the obtained cluster model becomes $Al_{13}O_{40}H_{41}$. Figure S2 (a) shows the labels of the O atoms of the bare cluster in which no equivalent O atom exists due to asymmetry. For the bare cluster, H atom is already bonded to the O atoms at A, B, C, D, F, G, H, J, M, P, R, S, T, d, f, g, and p. The sites for further hydrogen termination are determined based on the molecular orbital coefficients. Two H atoms are bonded to the O atoms at E and o because of the large coefficients of the LUMO (Fig. S2 (b)). In a similar manner, two H atoms are bonded to the O atoms at C and g, i and r, M and h, j and o, Q and m, I and q, I and N, R and r, T and U, A and a, and s and t based on the coefficients of the LUMO+1, +2, +3, +4, +5, +6, +7, +8, +9, +10, and +11, respectively (Fig. S2 (c)–(m)). The O atoms at the vertex of the tetrahedral Al species, i.e. K, L, O, k, ℓ, are not terminated because the coefficients of theses O atoms are small, which is the same situation as in the slab model.

Figure 7 (a) illustrates the SSHT cluster model after the geometry optimization of the cluster model obtained above. This model has an appropriate wide energy gap of 5.4 eV corresponding with experiments (Fig. S3). The O atoms at A, C, I, M, S, T, g, o, and r are terminated with two H atoms, i.e., H_2O is adsorbed on the boundary surface. Therefore, in
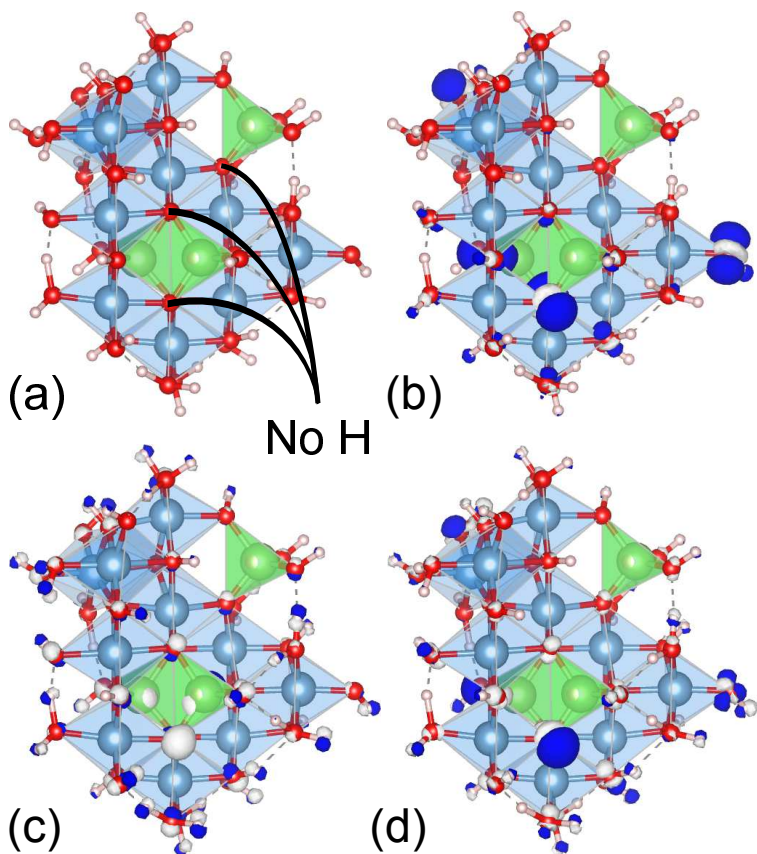
Figure 7: (a) SSHT cluster model of the γ-alumina (110) surface after the geometry optimization, and its (b) electron density difference, $\Delta\rho(\boldsymbol{x})$, (c) potential derivative, $v_\xi(\boldsymbol{x})$, and (d) VCD, $\eta_\xi(\boldsymbol{x})$. Isosurface values of $\Delta\rho(\boldsymbol{x})$, $v_\xi(\boldsymbol{x})$, and $\eta_\xi(\boldsymbol{x})$ are 3.0×10^{-3}, 7.0×10^{-3}, and 2.0×10^{-5} a.u., respectively.

contrast to the slab model, hydrogen bonds exist at the edge of the cluster model. Cartesian coordinates of the SSHT cluster model are tabulated in Table S2.

Regioselectivity of the Cu and NO Adsorption.

The VCD analysis for the γ-alumina cluster model was performed to identify a Cu^{2+} adsorption site (Figs. 6 (b)–(d)). $\Delta\rho(\boldsymbol{x})$ is distributed on a few O atoms located at the center and edge of the model. Therefore, the adsorption sites are ambiguous based on the frontier orbital theory. In contrast, $v_\xi(\boldsymbol{x})$ also has large values on the central O atom. Consequently, $\eta_\xi(\boldsymbol{x})$, which is given by the product of $\Delta\rho(\boldsymbol{x})$ and $v_\xi(\boldsymbol{x})$, is localized on the central O atom at the vertex of the tetrahedral Al species. Therefore, $\eta_\xi(\boldsymbol{x})$ clarifies the regioselectivity more

15

clearly than $\Delta\rho(\boldsymbol{x})$. Notably, the O atom where $\eta_\xi(\boldsymbol{x})$ is localized is not terminated with H atoms. The O atom without a hydrogen termination has a lone electron pair and acts as a Lewis base.[16] Thus, this site can be the adsorption site of $Cu(OH)_2$.

The OVCCs were calculated to determine molecular orbitals mainly contributing to the interactions of the surface with $Cu(OH)_2$ (Table S1). The OVCC of the HOMO has the largest value, which suggests that the HOMO mainly contributes to the reaction with $Cu(OH)_2$. This is because the HOMO and its orbital vibronic coupling density (OVCD), the density form of the OVCC, have large values on the Lewis-basic O atom (Figs. S4 (a) and (b)). The second and third largest OVCCs are for the HOMO-2 and HOMO-1, respectively. These orbitals are also distributed on the Lewis-basic site (Figs. S4 (c)–(f)), and moderately contribute to the reaction with $Cu(OH)_2$.
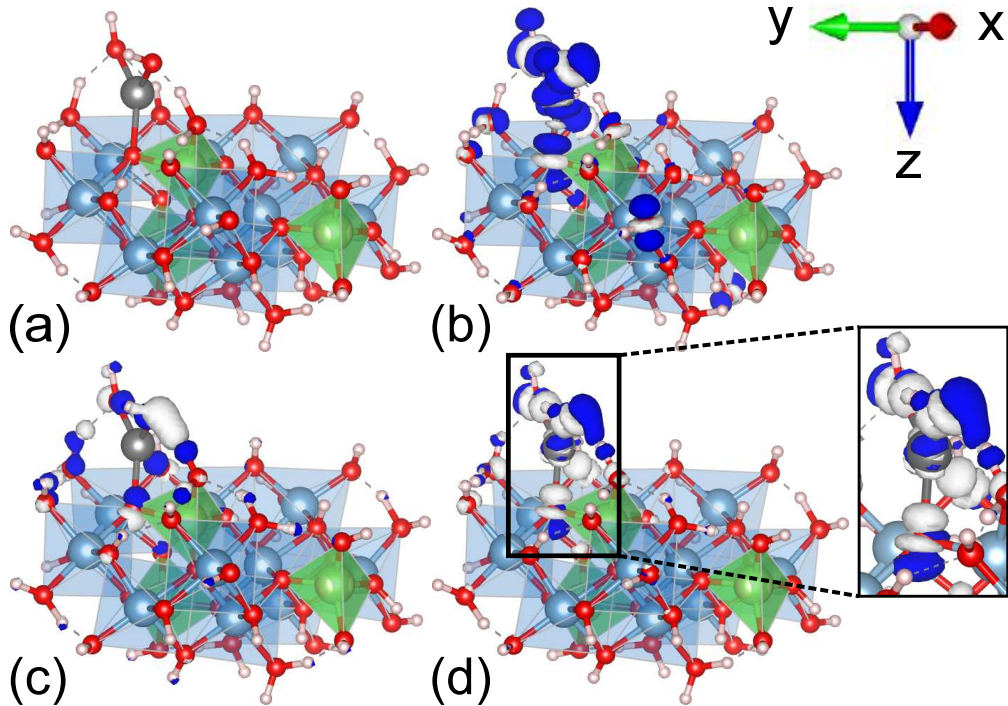

Figure 8: (a) Geometry-optimized structure of the $Cu(OH)_2/\gamma$-alumina cluster model, and its (b) electron density difference, $\Delta\rho(\boldsymbol{x})$, (c) potential derivative, $v_\xi(\boldsymbol{x})$, and (d) VCD, $\eta_\xi(\boldsymbol{x})$. Isosurface values of $\Delta\rho(\boldsymbol{x})$, $v_\xi(\boldsymbol{x})$, and $\eta_\xi(\boldsymbol{x})$ are 3.0×10^{-3}, 7.0×10^{-3}, and 2.0×10^{-5} a.u., respectively.

Figure 8 (a) illustrates the geometry-optimized structure of the $Cu(OH)_2/\gamma$-alumina

model predicted by the above VCD analysis. The optimization exhibits that $Cu(OH)_2$ adsorbs on the Lewis-basic O atom. The VCD analysis for the $Cu(OH)_2/\gamma$-alumina model was performed to identify an NO adsorption site (Figs 8 (b)–(d)). Since NO is predicted to be adsorb on the sites where the VCD is localized in $Cu(OH)_2$ because $\Delta\rho(\boldsymbol{x})$, $v_\xi(\boldsymbol{x})$, and $\eta_\xi(\boldsymbol{x})$ are localized on $Cu(OH)_2$. $\eta_\xi(\boldsymbol{x})$ is distributed not only on $Cu(OH)_2$ but also on the Lewis-basic O atom of the γ-alumina surface. This indicates that the excessive reaction energies arising from the NO adsorption dissipate to the γ-alumina surface. In other words, the catalyst support can be regarded as a heat bath. In addition, $Cu(OH)_2$ can be tightly bonded on the γ-alumina surface because of the localization of $\eta_\xi(\boldsymbol{x})$ on the Lewis-basic site, which results in the highly dispersed Cu^{2+} species. This is so-called anchoring effect.

Figure 9 (a) illustrates the geometry optimized structure of the NO-adsorbed $Cu(OH)_2/\gamma$-alumina model where the geometry optimization was started from the structure in which NO is placed on the site where the VCD is localized. To manifest the validity of the VCD as a reactivity index, the geometry optimizations were also performed where the initial NO positions are changed on the $Cu(OH)_2/\gamma$-alumina model. Consequently, the optimized structure predicted by the VCD analysis is discovered to be the most energetically stable (Fig. S5). Therefore, the regioselectivity of the NO adsorption in the present model is successfully reproduced via the VCD analysis.

The VCD analysis of the NO-adsorbed $Cu(OH)_2/\gamma$-alumina model was performed to identify a second NO adsorption site (Figs 9 (b)–(d)). $\Delta\rho(\boldsymbol{x})$ is delocalized over the NO, $Cu(OH)_2$, and γ-alumina. Thus, the site for the second NO adsorption is ambiguous as long as only the electronic state is considered. In contrast, $v_\xi(\boldsymbol{x})$ is mainly distributed on the first NO. Therefore, $\eta_\xi(\boldsymbol{x})$ is localized on the NO that is previously adsorbed on the $Cu(OH)_2/\gamma$-alumina model, and the second NO is predicted to be adsorbed towards the first NO. Again, $\eta_\xi(\boldsymbol{x})$ clarifies the regioselectivity more clearly than $\Delta\rho(\boldsymbol{x})$. Figure 9 (d) illustrates the geometry-optimized structure of the $Cu(OH)_2/\gamma$-alumina model with the two NO molecules adsorbed. The NO molecules undergo dimerization on $Cu(OH)_2$. The distance
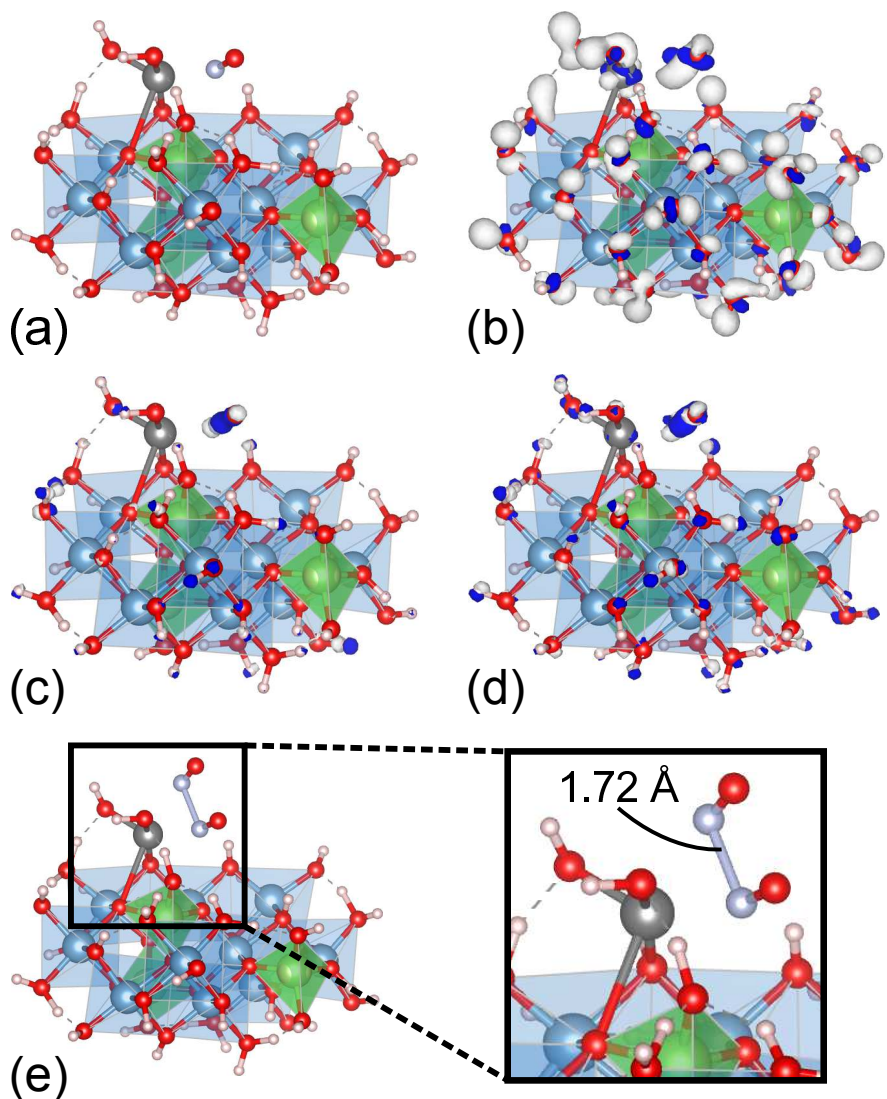
17

Figure 9: (a) Geometry-optimized structure of the NO-adsorbed $Cu(OH)_2/\gamma$-alumina cluster model, and its (b) electron density difference, $\Delta\rho(\boldsymbol{x})$, (c) potential derivative, $v_\xi(\boldsymbol{x})$, and (d) VCD, $\eta_\xi(\boldsymbol{x})$. Isosurface values of $\Delta\rho(\boldsymbol{x})$, $v_\xi(\boldsymbol{x})$, and $\eta_\xi(\boldsymbol{x})$ are 7.0×10^{-2}, 1.0×10^{-2}, and 5.0×10^{-4} a.u., respectively. (e) Geometry-optimized structure of the $Cu(OH)_2/\gamma$-alumina model with the two NO molecules adsorbed.

between the N atoms is 1.72 , which is sufficiently close to form a N–N bond.

The IR spectrum of the γ-alumina cluster model as well as the UV/Vis spectrum of the $Cu(OH)_2/\gamma$-alumina cluster model were calculated to check the reliability of the models discussed thus far. Figure 10 (a) shows the simulated and experimental IR spectra. The γ-alumina cluster model is considered to be realistic because the lineshape of the simulated IR spectrum appropriately reproduces that of the experimental spectrum. The observed IR
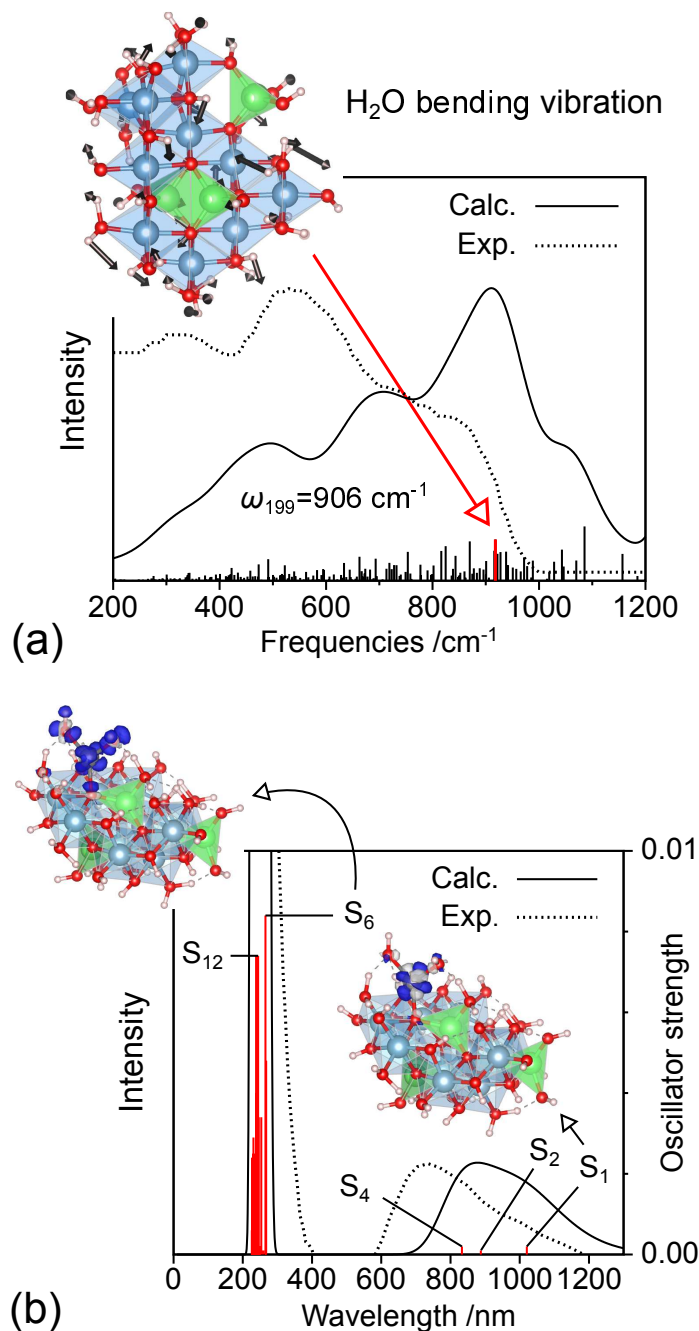
H$_2$O bending vibration

ω_{199}=906 cm^{-1}

(a)

(b)

Figure 10: (a) Simulated IR spectrum of the γ-alumina cluster model where the linewidth of the Gaussian function is 40 cm^{-1}. Inset shows vibrational mode 199. Experimental IR spectrum treated at 600°C is obtained from Ref. 45. (b) Simulated UV/Vis spectrum of the Cu(OH)$_2$/γ-alumina cluster model with the excited electronic states from S$_1$ to S$_{25}$ considered. The linewidth of the Gaussian function is 1000 cm^{-1}. Inset shows the electron density difference between S$_1$ and S$_0$ as well as S$_6$ and S$_0$. Experimental UV/Vis spectrum is obtained from Ref. 10.

spectrum in the ranging from 200 to 1200 cm^{-1} is assigned to the H_2O bending vibrations based on the calculation. Figure 10 (b) shows the simulated and experimental UV/Vis spectrum. The lineshape of the simulated UV/Vis spectrum also appropriately reproduces that of the experimental spectrum, and this indicates that the $Cu(OH)_2/\gamma$-alumina cluster model is realistic. The observed spectrum ranging from 600 to 1200 nm is attributed to the absorption of S_1, S_2, and S_4. The electron density difference between S_1 and S_0 is localized on the Cu atom with the d orbital distributions. Similar electron density differences are obtained between S_2 and S_0 as well as S_4 and S_0 (Fig. S6 (a)–(c)). Therefore, the absorption in this region is assigned to the d-d transitions of the Cu atom. The observed spectrum below 400 nm is mainly attributed to the absorption of S_6 and S_{12}. The electron density differences between S_6 and S_0 as well as S_{12} and S_0 are distributed over $Cu(OH)_2$ (Figs. S6 (d) and (e)).

The geometry-optimized structures were also obtained using the slab models (Figs. S7 (a)–(c)). These optimized structures are in good agreement with those using the cluster models. Therefore, the cluster models appropriately reproduce the Cu and NO adsorptions on the slab models.

It has been reported by experiments that the tetrahedral Al species transform the structure by the Cu loading.[12] Hence, the interatomic distance and Mulliken charge of the tetrahedral Al species on which $Cu(OH)_2$ is adsorbed were computed (Fig. S8 and Table S4). As a result of the Cu adsorption on the γ-alumina cluster model, the distance between Al and O bonded to Cu is increased from 1.757 to 1.823 , whereas the other three Al–O distances remain unchanged. In addition, the Mulliken charge of Al is increased from +0.928 to +1.043. This trend is the same in the slab model (Table S4). These results indicate that one of the Al–O distances in the tetrahedral Al species is increased by the electron transfer from the γ-alumina to Cu. To explain this behavior, the orbital levels of the geometry-optimized AlO_4 with the T_d symmetry were calculated (Fig. S9). Five electrons should be given to AlO_4 for satisfying the appropriate oxidation number because the formal charge of Al is 3+ and of

O is 2−, The HOMO with the T_1 symmetry is the three-fold degenerate. The symmetrical product of T_1 is determined as follows:

$$[T_1^2] = A_1 \oplus E \oplus T_2. \tag{14}$$

In addition, the VCC of the t_2 modes are the largest except for the totally-symmetric a_1 mode (Table S5). Thus, the electron drawing from the HOMO induces the $T \otimes t_2$ Jahn–Teller distortion.[54] The Jahn–Teller distortion in the t_2 modes lowers the symmetry of the tetrahedron to C_{3v},[55] which rationalizes the elongation of one of the Al–O bonds in the tetrahedral Al species upon Cu adsorption.

Orbital Levels of the NO- and O_2-Adsorbed Cu/γ-Alumina.

The fragment orbital analyses were performed within the extended Hückel theory to investigate the role of the catalyst and its support. Figure 11 (a) illustrates the decomposition of the orbitals of the $Cu(OH)_2$/γ-alumina cluster model into those of $Cu(OH)_2$ and γ-alumina fragments. The singly occupied molecular orbital (SOMO) of the $Cu(OH)_2$/γ-alumina is raised with respect to that of the isolated $Cu(OH)_2$ because of the orbital interactions of the isolated $Cu(OH)_2$ with the γ-alumina. The main components of the SOMO of the $Cu(OH)_2$/γ-alumina are the SOMO of the $Cu(OH)_2$ (P_{km}=68.1%) and the HOMO-12 of the γ-alumina (3.4%). The orbitals exhibiting the second largest contribution in the γ-alumina is the HOMO-20 (0.7%), whose ratio is significantly smaller than the HOMO-12. Thus, the HOMO-12 mainly contributes to the interactions with $Cu(OH)_2$. This is because the HOMO-12 have large values on the Lewis-basic O atom.

Figure 11 (b) illustrates the decomposition of the orbitals of the NO-adsorbed $Cu(OH)_2$/γ-alumina model into those of NO and $Cu(OH)_2$/γ-alumina fragments. The HOMO of the NO-adsorbed $Cu(OH)_2$/γ-alumina, which is distributed over the $Cu(OH)_2$ and NO, mainly consists of the SOMOs of the $Cu(OH)_2$/γ-alumina and NO. Since the SOMO of the $Cu(OH)_2$/γ-
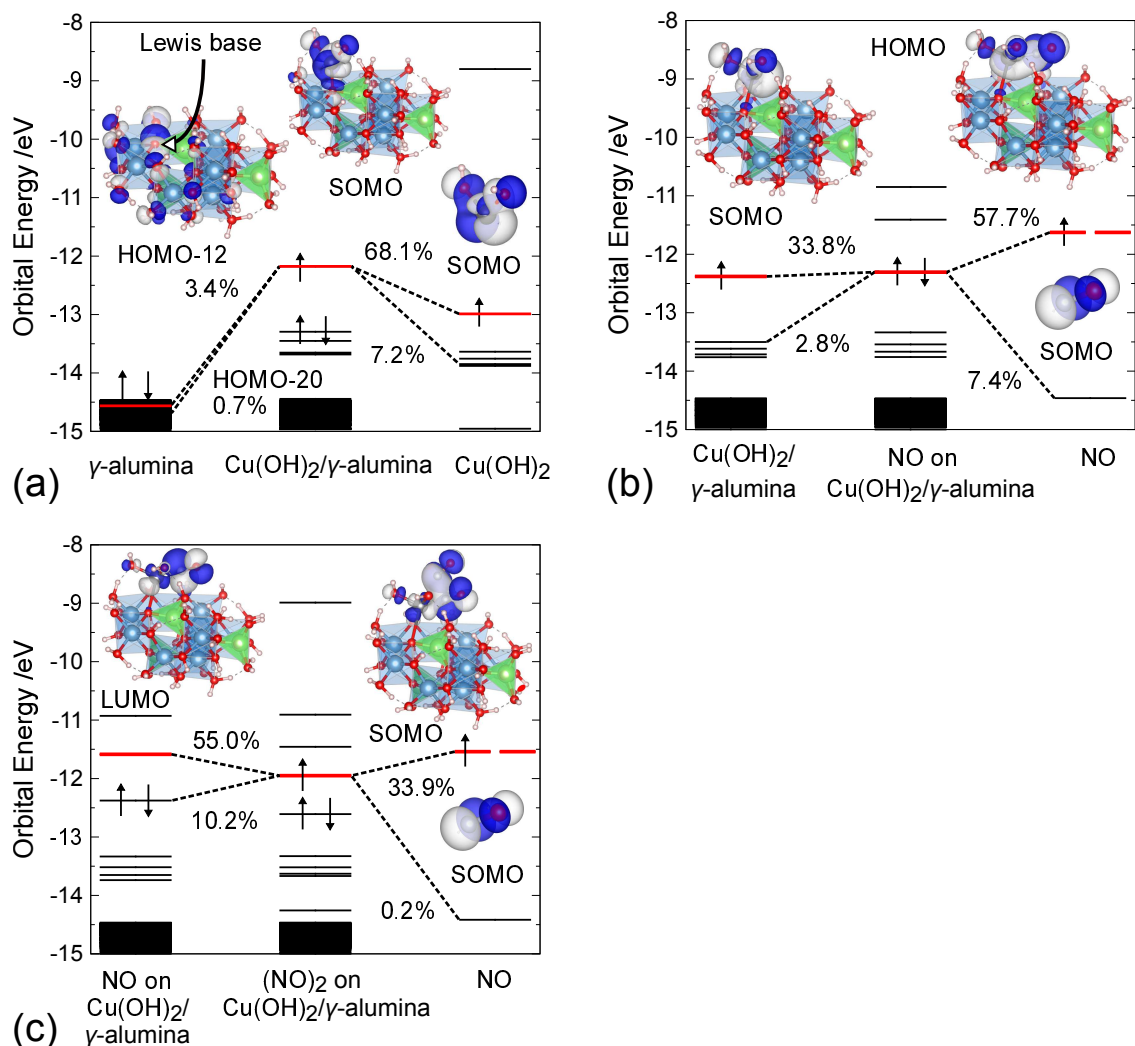
Figure 11: Fragment orbital analyses of the (a) $Cu(OH)_2/\gamma$-alumina, (b) NO-adsorbed $Cu(OH)_2/\gamma$-alumina, and (c) $(NO)_2$-adsorbed $Cu(OH)_2/\gamma$-alumina cluster models. Inset shows the molecular orbitals. Values of P_{km} are provided in percentages.

alumina is energetically close to that of NO, the electron transfer between them can occur. This is because the γ-alumina support raises the SOMO of the $Cu(OH)_2$. Therefore, the role of the catalyst support is to shift the frontier orbital levels of the catalyst. In addition, the γ-alumina hardly interacts with NO because the occupied orbitals of the γ-alumina are significantly lower than the SOMO of NO. This corresponds with the experimental observations that the γ-alumina itself exhibits the low catalytic activity for the NO reduction.[9]

Figure 11 (c) illustrates the decomposition of the orbitals of the $(NO)_2$-adsorbed $Cu(OH)_2/\gamma$-alumina model into those of NO and NO-adsorbed $Cu(OH)_2/\gamma$-alumina fragments. The

LUMO of the NO-adsorbed $Cu(OH)_2/\gamma$-alumina mainly interacts with the SOMO of NO. The SOMO of the $(NO)_2$-adsorbed $Cu(OH)_2/\gamma$-alumina has the N–N bonding and N–O anti-bonding, which is a characteristic of the $(NO)_2$ 2π orbital. The Mulliken charge of $(NO)_2$ on the $Cu(OH)_2/\gamma$-alumina was calculated to be -0.26. Therefore, the electron back-donation occurs from the $Cu(OH)_2/\gamma$-alumina to $(NO)_2$. This results in the occupation of the $(NO)_2$ 2π orbital, which can be the driving force of the NO reduction to N_2.

Finally, the orbital levels of the NO- and O_2-adsorbed $Cu(OH)_2/\gamma$-alumina were compared to show the ease of the NO adsorption on the Cu/γ-alumina under the oxidative condition. The geometries of the O_2-adsorbed $Cu(OH)_2/\gamma$-alumina were optimized using the cluster and slab models, which have similar structures where O_2 is adsorbed on $Cu(OH)_2$ (Figs S10 (a) and (b)). Figures S11 (a) and (b) present the results of the fragment orbital analyses of the NO- and O_2-adsorbed $Cu(OH)_2/\gamma$-alumina cluster models. The HOMO of the NO-adsorbed $Cu(OH)_2/\gamma$-alumina has the bonding character between Cu and NO, whereas the SOMO of the O_2-adsorbed $Cu(OH)_2/\gamma$-alumina has the anti-bonding character between Cu and O_2. This difference appears in the interatomic distance between Cu and NO or O_2, where the calculated Cu–N bond (1.775 Å) is shorter than the Cu–O bond (1.963 Å). The bond order between atom X and Y, which quantifies the strength of bond, is defined as follows:

$$\sum_{\mu \in X} \sum_{\nu \in Y} \sum_i n_i C_{\mu i}^* C_{\nu i} S_{\mu \nu}, \tag{15}$$

where n_i denotes the electron occupation number of molecular orbital i, $C_{\mu i}$ the i-th molecular orbital coefficient of atomic orbital μ belonging to X, and $S_{\mu \nu}$ the overlap integral between μ and ν. The bond orders of the Cu–N and Cu–O bonds were respectively computed to be 0.2741 and 0.1144, which indicates that the Cu–N bond is stronger than the Cu–O bond. This suggests that the curvature of the potential energy surface of the O_2-adsorbed $Cu(OH)_2/\gamma$-alumina with respect to the Cu-O distance is larger than that of the NO-adsorbed $Cu(OH)_2/\gamma$-alumina with respect to the Cu-N distance. In other words, the Cu–O bond is considered to be weakly bounded due to the small force constant and, therefore,

easy to dissociate. Notably, the stabilization energy resulting from the orbital interactions of the $Cu(OH)_2/\gamma$-alumina with NO (-2.730 eV) is comparable to that with O_2 (-2.812 eV). Thus, the depth of the potential energy surface of the NO- and O_2-adsorbed $Cu(OH)_2/\gamma$-alumina are assumed to be nearly equal.

Conclusions

On the basis of the DFT calculations using the computational models for the solid surface, we investigated the regioselectivity of the Cu adsorption on the γ-alumina surface and that of the NO adsorption on the Cu/γ-alumina surface as well as the role of the γ-alumina support on the NO reduction. The SSHT slab and cluster models of the γ-alumina surface, where the reactive sites for the hydrogen termination are determined based on the crystal and molecular orbital coefficients, reflect the experimental energy gap as well as the IR and UV/Vis spectra. The obtained models have O, OH, and H_2O on the surfaces. Notably, the SSHT procedure contains an arbitrariness on deciding the sites for the hydrogen termination when a few O atoms have orbital coefficients with similar magnitudes. However, it is expected even on the real surface that the adsorption sites are not uniquely determined due to the amorphous structure. Thus, this approach provides one way to determine the hydrogen termination sites on the metal oxide surfaces. These sites can also be determined utilizing the VCD as a reactivity index, although in the current study the orbital coefficients were used for simplicity.

The regioselectivity of the Cu adsorption on the γ-alumina surface and that of the NO adsorption on the Cu/γ-alumina surface were elucidated by the VCD theory more clearly than by the frontier orbital theory because of the localization of the vibrational states. The anchor site for $Cu(OH)_2$ was determined to be the O atom located in the tetrahedral sites of the γ-alumina surface. This O atom, which is not terminated with H atom, has a lone pair and serves as the Lewis base. The tetrahedral Al species transforms the structure upon the

Cu loading due to the Jahn–Teller distortion induced by the electron transfer from the Al species to Cu. The VCD analyses demonstrate that the NO adsorbs on the $Cu(OH)_2$, and the second NO successively adsorbs on the initially adsorbed NO. Namely, the dimerization of NO occurs on $Cu(OH)_2$. The adsorption of NO on the Cu/γ-alumina easily occurs compared with O_2 because of the strongly bounded Cu–NO bond.

The role of the γ-alumina support is discovered to raise the SOMO of the Cu catalyst, which promotes the electron transfer from the Cu/γ-alumina to NO because of the small orbital energy gap between them. Consequently, the orbital of $(NO)_2$ with the N–N bonding and N–O anti-bonding is occupied by electrons, and this is considered to be the driving force of the NO reduction. Another role of the γ-alumina support is to bond the $Cu(OH)_2$ on its surface to inhibit the catalyst aggregations. In addition, the support acts as a heat bath for dissipating the excessive reaction energies due to the NO adsorption and reduction. These roles of the catalyst support can be regarded as the anchoring effect.

Acknowledgement

Supporting Information Available

The following files are available free of charge. Band structure of the SSHT slab model; Cartesian coordinates of the SSHT slab model; molecular orbitals of the bare cluster; orbital levels of the SSHT cluster model; Cartesian coordinates of the SSHT cluster model; OVCCs

and OVCD of the γ-alumina cluster model; geometry-optimized structures of the NO-adsorbed Cu(OH)$_2$/γ-alumina cluster model; electron density differences of the Cu(OH)$_2$/γ-alumina cluster model; geometry-optimized structures using the slab models; atomic labels of the tetrahedral Al species; interatomic distance and Mulliken charge of the tetrahedral Al species; orbital levels of AlO$_4$; VCCs of AlO$_4$; geometry-optimized structures of the O$_2$-adsorbed Cu(OH)$_2$/γ-alumina; fragment orbital analyses of the NO- and O$_2$-adsorbed Cu(OH)$_2$/γ-alumina.

References

(1) Kašpar, J.; Fornasiero, P.; Hickey, N. Automotive catalytic converters: current status and some perspectives. Catal. Today **2003**, 77, 419–449.

(2) Shelef, M.; Graham, G. Why rhodium in automotive three-way catalysts? Catal. Rev. **1994**, 36, 433–457.

(3) Brown, W. A.; King, D. A. NO chemisorption and reactions on metal surfaces: a new perspective. J. Phys. Chem. B **2000**, 104, 2578–2595.

(4) Deushi, F.; Ishikawa, A.; Nakai, H. Density Functional Theory Analysis of Elementary Reactions in NO$_x$ Reduction on Rh Surfaces and Rh Clusters. J. Phys. Chem. C **2017**, 121, 15272–15281.

(5) Ishikawa, A.; Tateyama, Y. First-Principles Microkinetic Analysis of NO+CO Reactions on Rh (111) Surface toward Understanding NO$_x$ Reduction Pathways. J. Phys. Chem. C **2018**, 122, 17378–17388.

(6) Takagi, N.; Ishimura, K.; Fukuda, R.; Ehara, M.; Sakaki, S. Reaction Behavior of the NO Molecule on the Surface of an M n Particle (M= Ru, Rh, Pd, and Ag; n=13 and 55): Theoretical Study of Its Dependence on Transition-Metal Element. J. Phys. Chem. A **2019**, 123, 7021–7033.

(7) Ward, T. R.; Alemany, P.; Hoffmann, R. Adhesion of rhodium, palladium, and platinum to alumina and the reduction of nitric oxide on the resulting surfaces: a theoretical analysis. J. Phys. Chem. **1993**, 97, 7691–7699.

(8) Ward, T. R.; Hoffmann, R.; Shelef, M. Coupling nitrosyls as the first step in the reduction of NO on metal surfaces: the special role of rhodium. Surf. Sci. **1993**, 289, 85–99.

(9) Yamamoto, T.; Tanaka, T.; Kuma, R.; Suzuki, S.; Amano, F.; Shimooka, Y.; Kohno, Y.; Funabiki, T.; Yoshida, S. NO reduction with CO in the presence of O_2 over Al_2O_3-supported and Cu-based catalysts. Phys. Chem. Chem. Phys. **2002**, 4, 2449–2458.

(10) Yamamoto, T.; Tanaka, T.; Suzuki, S.; Kuma, R.; Teramura, K.; Kou, Y.; Funabiki, T.; Yoshida, S. NO reduction with CO in the presence of O_2 over Cu/Al_2O_3 (3)–structural analysis of active species by means of XAFS and UV/VIS/NIR spectroscopy. Top. Catal. **2002**, 18, 113–118.

(11) Amano, F.; Suzuki, S.; Yamamoto, T.; Tanaka, T. One-electron reducibility of isolated copper oxide on alumina for selective NO–CO reaction. Appl. Catal. B: Environ. **2006**, 64, 282–289.

(12) Hosokawa, S.; Matsuki, K.; Tamaru, K.; Oshino, Y.; Aritani, H.; Asakura, H.; Teramura, K.; Tanaka, T. Selective reduction of NO over Cu/Al_2O_3: Enhanced catalytic activity by infinitesimal loading of Rh on Cu/Al_2O_3. Molecular Catalysis **2017**, 442, 74–82.

(13) Fukuda, R.; Sakai, S.; Takagi, N.; Matsui, M.; Ehara, M.; Hosokawa, S.; Tanaka, T.; Sakaki, S. Mechanism of NO–CO reaction over highly dispersed cuprous oxide on γ-alumina catalyst using a metal–support interfacial site in the presence of oxygen: similarities to and differences from biological systems. Catal. Sci. Technol. **2018**, 8, 3833–3845.

(14) Nagai, Y.; Hirabayashi, T.; Dohmae, K.; Takagi, N.; Minami, T.; Shinjoh, H.; Matsumoto, S. Sintering inhibition mechanism of platinum supported on ceria-based oxide and Pt-oxide–support interaction. J. Catal. **2006**, 242, 103–109.

(15) Machida, M.; Minami, S.; Ikeue, K.; Hinokuma, S.; Nagao, Y.; Sato, T.; Nakahara, Y. Rhodium nanoparticle anchoring on $AlPO_4$ for efficient catalyst sintering suppression. Chem. Mater. **2014**, 26, 5799–5805.

(16) Trueba, M.; Trasatti, S. P. γ-alumina as a support for catalysts: a review of fundamental aspects. Eur. J. Inorg. Chem. **2005**, 17, 3393–3403.

(17) Fukui, K.; Yonezawa, T.; Shingu, H. A molecular orbital theory of reactivity in aromatic hydrocarbons. J. Chem. Phys. **1952**, 20, 722–725.

(18) Fukui, K. Role of frontier orbitals in chemical reactions. Science **1982**, 218, 747–754.

(19) Sato, T.; Tokunaga, K.; Tanaka, K. Vibronic coupling in naphthalene anion: vibronic coupling density analysis for totally symmetric vibrational modes. J. Phys. Chem. A **2008**, 112, 758–767.

(20) Kojima, Y.; Ota, W.; Teramura, K.; Hosokawa, S.; Tanaka, T.; Sato, T. Model building of metal oxide surfaces and vibronic coupling density as a reactivity index: Regioselectivity of CO_2 adsorption on Ag-loaded Ga_2O_3. Chem. Phys. Lett. **2019**, 715, 239–243.

(21) Ota, W.; Teramura, K.; Hosokawa, S.; Tanaka, T.; Sato, T. Regioselectivity of H_2 adsorption on Ga_2O_3 surface based on vibronic coupling density analysis. J. Comput. Chem. Jpn. **2018**, 17, 138–141.

(22) Sato, T.; Iwahara, N.; Haruta, N.; Tanaka, K. C_{60} bearing ethylene moieties. Chem. Phys. Lett. **2012**, 531, 257–260.

(23) Haruta, N.; Sato, T.; Tanaka, K. Chemical reactivity in nucleophilic cycloaddition to

C_{70}: vibronic coupling density and vibronic coupling constants as reactivity indices. J. Org. Chem. **2012**, 77, 9702–9706.

(24) Haruta, N.; Sato, T.; Iwahara, N.; Tanaka, K. Vibronic couplings in cycloadditions to fullerenes. J. Phys.: Conf. Ser. **2013**, 428, 012003.

(25) Haruta, N.; Sato, T.; Tanaka, K. Regioselectivity in multiple cycloadditions to fullerene C_{60}: vibronic coupling density analysis. Tetrahedron **2014**, 70, 3510–3513.

(26) Haruta, N.; Sato, T.; Tanaka, K. Reactivity of endohedral metallofullerene $La_2@C_{80}$ in nucleophilic and electrophilic attacks: vibronic coupling density approach. J. Org. Chem. **2014**, 80, 141–147.

(27) Haruta, N.; Sato, T.; Tanaka, K. Reactivity index for Diels–Alder cycloadditions to large polycyclic aromatic hydrocarbons using vibronic coupling density. Tetrahedron Lett. **2015**, 56, 590–594.

(28) Hoffman, R. Solids and Surfaces: A Chemist's View of Bonding in Extended Structures; VCH: New York, 1988.

(29) Sato, T.; Tokunaga, K.; Iwahara, N.; Shizu, K.; Tanaka, K. Vibronic Coupling Constant and Vibronic Coupling Density. In The Jahn-Teller Effect: Fundamentals and Implications for Physics and Chemistry; Köppel, H., Yarkony, D. R., Barentzen, H., Eds.; Springer-Verlag: Berlin and Hidelberg, 2009; pp 99–129.

(30) Sato, T.; Uejima, M.; Iwahara, N.; Haruta, N.; Shizu, K.; Tanaka, K. Vibronic coupling density and related concepts. J. Phys.: Conf. Ser. **2013**, 428, 012010.

(31) Fischer, G. Vibronic Coupling: The Interaction between the Electronic and Nuclear Motions; Academic Press: London, 1984.

(32) Azumi, T.; Matsuzaki, K. What Does the Term "Vibronic Coupling" Mean? Photochem. Photobiol. **1977**, 25, 315–326.

(33) Hellmann, H. Einführung in die Quantenchemie; Deuticke and Company: Leipzog, 1937.

(34) Feynman, R. P. Forces in molecules. Phys. Rev. **1939**, 56, 340–343.

(35) Parr, R. G.; Yang, W. Density functional approach to the frontier-electron theory of chemical reactivity. J. Am. Chem. Soc. **1984**, 106, 4049–4050.

(36) Parr, R. G.; Yang, W. Density-Functional Theory of Atoms and Molecules; Oxford University Press: New York, 1994.

(37) Hoffmann, R.; Fujimoto, H.; Swenson, J. R.; Wan, C.-C. Theoretical aspects of the bonding in some three-membered rings containing sulfur. J. Am. Chem. Soc. **1973**, 95, 7644–7650.

(38) Krokidis, X.; Raybaud, P.; Gobichon, A.-E.; Rebours, B.; Euzen, P.; Toulhoat, H. Theoretical study of the dehydration process of boehmite to γ-alumina. J. Phys. Chem. B **2001**, 105, 5121–5130.

(39) Digne, M.; Sautet, P.; Raybaud, P.; Euzen, P.; Toulhoat, H. Hydroxyl groups on γ-alumina surfaces: A DFT study. J. Catal. **2002**, 211, 1–5.

(40) Digne, M.; Sautet, P.; Raybaud, P.; Euzen, P.; Toulhoat, H. Use of DFT to achieve a rational understanding of acid–basic properties of γ-alumina surfaces. J. Catal. **2004**, 226, 54–68.

(41) Nortier, P.; Fourre, P.; Saad, A. M.; Saur, O.; Lavalley, J. Effects of crystallinity and morphology on the surface properties ofalumina. App. Catal. **1990**, 61, 141–160.

(42) Morterra, C.; Magnacca, G. A case study: surface chemistry and surface structure of catalytic aluminas, as studied by vibrational spectroscopy of adsorbed species. Catal. Today **1996**, 27, 497–532.

(43) Busca, G.; Lorenzelli, V.; Ramis, G.; Willey, R. J. Surface sites on spinel-type and corundum-type metal oxide powders. Langmuir **1993**, 9, 1492–1499.

(44) Tsyganenko, A. A.; Mardilovich, P. P. Structure of alumina surfaces. J. Chem. Soc., Faraday Trans. **1996**, 92, 4843–4852.

(45) Pecharroman, C.; Sobrados, I.; Iglesias, J.; Gonzalez-Carreno, T.; Sanz, J. Thermal evolution of transitional aluminas followed by NMR and IR spectroscopies. J. Phys. Chem. B **1999**, 103, 6160–6170.

(46) Paglia, G.; Buckley, C. E.; Udovic, T. J.; Rohl, A. L.; Jones, F.; Maitland, C. F.; Connolly, J. Boehmite-derived γ-alumina system. 2. Consideration of hydrogen and surface effects. Chem. Mater. **2004**, 16, 1914–1923.

(47) Frisch, M. J.; Trucks, G. W.; Schlegel, H. B.; Scuseria, G. E.; Robb, M. A.; Cheeseman, J. R.; Scalmani, G.; Barone, V.; Mennucci, B.; Petersson, G. A.; Nakatsuji, H.; Caricato, M.; Li, X.; Hratchian, H. P.; Izmaylov, A. F.; Bloino, J.; Zheng, G.; Sonnenberg, J. L.; Hada, M.; Ehara, M.; Toyota, K.; Fukuda, R.; Hasegawa, J.; Ishida, M.; Nakajima, T.; Honda, Y.; Kitao, O.; Nakai, H.; Vreven, T.; Montgomery Jr., J. A.; Peralta, J. E.; Ogliaro, F.; Bearpark, B.; J, H. J.; Brothers, E.; Kudin, K. N.; Staroverov, V. N.; Keith, T.; Kobayashi, R.; Normand, J.; Raghavachari, K.; Rendell, A.; Burant, J. C.; Iyengar, S. S.; Tomasi, J.; Cossi, M.; Rega, N.; Millam, J. M.; Klene, M.; Knox, J. E.; Cross, J. B.; Bakken, V.; Adamo, C.; Jaramillo, J.; Gomperts, R.; Stratmann, R. E.; Yazyev, O.; Austin, A. J.; Cammi, R.; Pomelli, C.; Ochterski, J. W.; Martin, R. L.; Morokuma, K.; Zakrzewski, V. G.; Voth, G. A.; Salvador, P.; Dannenberg, J. J.; Dapprich, S.; Daniels, A. D.; Farkas, O.; Foresman, J. B.; Ortiz, J. V.; Cioslowski, J.; Fox, D. J. Gaussian 09, Revision D. 01, Gaussian, Inc.: Wallingford, CT, 2013.

(48) Frisch, M. J.; Trucks, G. W.; Schlegel, H. B.; Scuseria, G. E.; Robb, M. A.; Cheese-

man, J. R.; Scalmani, G.; Barone, V.; Mennucci, B.; Petersson, G. A.; Nakatsuji, H.; Caricato, M.; Li, X.; Hratchian, H. P.; Izmaylov, A. F.; Bloino, J.; Zheng, G.; Sonnenberg, J. L.; Hada, M.; Ehara, M.; Toyota, K.; Fukuda, R.; Hasegawa, J.; Ishida, M.; Nakajima, T.; Honda, Y.; Kitao, O.; Nakai, H.; Vreven, T.; Montgomery Jr., J. A.; Peralta, J. E.; Ogliaro, F.; Bearpark, B.; J, H. J.; Brothers, E.; Kudin, K. N.; Staroverov, V. N.; Keith, T.; Kobayashi, R.; Normand, J.; Raghavachari, K.; Rendell, A.; Burant, J. C.; Iyengar, S. S.; Tomasi, J.; Cossi, M.; Rega, N.; Millam, J. M.; Klene, M.; Knox, J. E.; Cross, J. B.; Bakken, V.; Adamo, C.; Jaramillo, J.; Gomperts, R.; Stratmann, R. E.; Yazyev, O.; Austin, A. J.; Cammi, R.; Pomelli, C.; Ochterski, J. W.; Martin, R. L.; Morokuma, K.; Zakrzewski, V. G.; Voth, G. A.; Salvador, P.; Dannenberg, J. J.; Dapprich, S.; Daniels, A. D.; Farkas, O.; Foresman, J. B.; Ortiz, J. V.; Cioslowski, J.; Fox, D. J. Gaussian 09, Revision E. 01, Gaussian, Inc.: Wallingford, CT, 2013.

(49) Hoffmann, R. An extended Hückel theory. I. hydrocarbons. J. Chem. Phys. **1963**, 39, 1397–1412.

(50) Landrum, G.; Glassey, W. Yet Another Extended Hückel Molecular Orbital Package (YAeHMOP). `http://yaehmop.sourceforge.net`.

(51) Te Velde, G.; Baerends, E. Precise density-functional method for periodic structures. Phys. Rev. B **1991**, 44, 7888.

(52) Te Velde, G.; Baerends, E. Numerical integration for polyatomic systems. J. Comput. Phys. **1992**, 99, 84–98.

(53) Ealet, B.; Elyakhloufi, M. H.; Gillet, E.; Ricci, M. Electronic and crystallographic structure of γ-alumina thin films. Thin Solid Films **1994**, 250, 92–100.

(54) Bersuker, I. B. The Jahn–Teller Effect; Cambridge University Press, 2006.

(55) Ceulemans, A.; Vanquickenborne, L. The epikernel principle. <u>Struct. Bonding</u> **1989**, <u>71</u>, 125–159.

Graphical TOC Entry
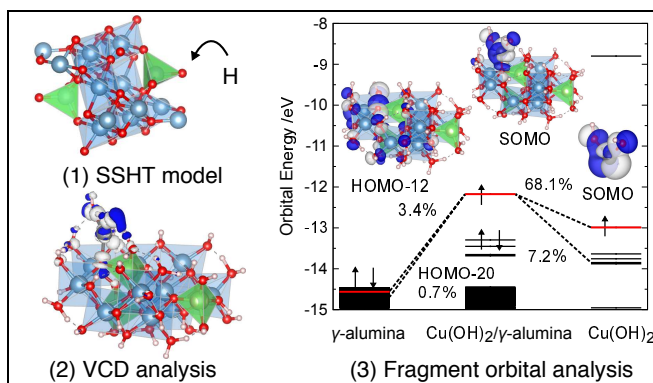
Supporting Information

Role of Catalyst Support and Regioselectivity of Molecular Adsorption on a Metal Oxide Surface: NO Reduction on Cu/γ-alumina

Wataru Ota[1,2], Yasuro Kojima[2], Saburo Hosokawa[2,3], Kentaro Teramura[2,3], Tsunehiro Tanaka[2,3], Tohru Sato[1,2,3]*

[1] *Fukui Institute for Fundamental Chemistry, Kyoto University, Sakyo-ku, Kyoto 606-8103, Japan*

[2] *Department of Molecular Engineering, Graduate School of Engineering, Kyoto University, Nishikyo-ku, Kyoto 615-8510, Japan*

[3] *Elements Strategy Initiative for Catalysts & Batteries (ESICB), Kyoto University, Kyotodaigaku Katsura, Nishikyo-ku, Kyoto 615-8245, Japan*
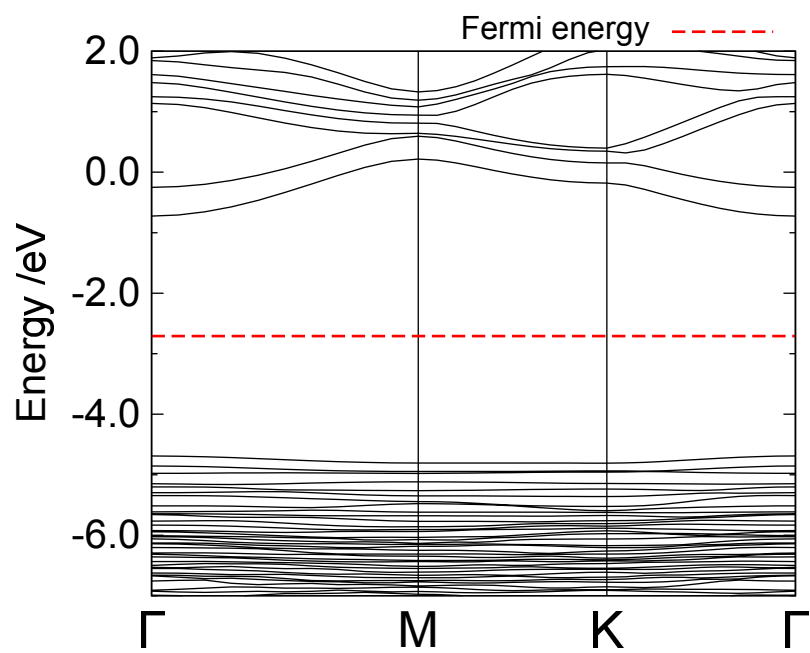
Figure S1. Calculated band structure of the SSHT slab model. The band gap is 3.97 eV.

Table S1. Cartesian coordinates of the SSHT slab model. Lattice vectors are (-8.0678, 0.0000, 0.0000) and (0.0000, 8.4130, 0.0000). The coordinates are provided in Angstrom units.

No.	Atom	x	y	z	No.	Atom	x	y	z
1	Al	-0.8532	-2.1445	-0.5612	33	O	1.3434	3.4186	-0.9256
2	Al	1.1183	2.1237	0.5174	34	O	-1.0954	-3.4306	0.9288
3	Al	-3.9268	2.0726	1.9764	35	O	-1.0606	-0.8853	0.9367
4	Al	-3.8845	-2.1163	-2.0309	36	O	1.3445	0.8895	-0.9797
5	Al	-0.7291	-2.1526	2.3045	37	O	3.0706	-0.7118	-2.0428
6	Al	0.9851	2.1587	-2.3391	38	O	-2.7743	0.7033	1.9970
7	Al	2.1827	-2.0494	0.6751	39	O	-2.8279	3.4682	2.0617
8	Al	-1.9200	2.1306	-0.6751	40	O	3.0547	-3.4826	-2.0462
9	Al	3.2610	0.6592	-0.8137	41	O	2.8364	2.0514	3.2291
10	Al	-2.9661	-0.6557	0.7554	42	O	-2.6166	-2.4034	-3.2768
11	Al	-2.9988	-3.5769	0.7977	43	O	-0.8803	-3.5822	3.4350
12	Al	3.2391	3.5990	-0.7783	44	O	-0.7107	-0.7036	3.4130
13	Al	1.1980	-3.4664	-2.1325	45	O	1.0240	0.7104	-3.4290
14	Al	-0.9425	3.4665	2.1387	46	O	1.1612	3.5945	-3.4700
15	Al	-0.8565	0.6350	2.0730	47	O	1.1027	-2.0526	-3.3691
16	Al	1.1586	-0.6416	-2.1244	48	O	-0.8946	2.0340	3.3624
17	O	1.1042	-2.4880	2.0387	49	H	-0.8990	-3.6873	4.4039
18	O	-0.8358	2.4934	-2.0475	50	H	-0.1868	-0.5600	4.2270
19	O	3.0532	2.1092	0.4986	51	H	-1.6305	1.9482	4.0115
20	O	-2.7804	-2.1103	-0.5342	52	H	1.2013	-3.5711	2.0778
21	O	1.0544	-2.0888	-0.7611	53	H	3.8205	2.1588	-2.8493
22	O	-0.7881	2.0931	0.7454	54	H	1.0212	0.5948	-4.3975
23	O	3.1987	2.1327	-2.0858	55	H	0.3266	-2.0683	-3.9760
24	O	-2.8919	-2.1045	2.0757	56	H	2.9879	2.0437	4.2012
25	O	0.9815	3.4223	1.9889	57	H	-2.7926	-2.4397	-4.2435
26	O	-0.7320	-3.4516	-1.9971	58	H	1.6861	0.8258	2.5299
27	O	-0.6912	-0.7763	-1.8274	59	H	-3.4662	-2.0932	2.8751
28	O	0.9784	0.7850	1.8281	60	H	-0.9186	3.6123	-2.0851
29	O	3.2683	-0.6428	0.5749	61	H	1.7686	3.7268	-4.2273
30	O	-2.9337	0.6544	-0.6651	62	H	-1.4400	-0.1669	-2.0215
31	O	-3.0102	3.5246	-0.5532	63	H	1.6000	3.0011	2.6990
32	O	3.2518	-3.4887	0.5769	64	H	-1.4481	-3.0488	-2.6881

(a)

(b) LUMO (E, o)

(c) LUMO+1 (C, g)

(d) LUMO+2 (i, r)

(e) LUMO+3 (M, h)

(f) LUMO+4 (j, o)

(g) LUMO+5 (Q, m)

(h) LUMO+6 (l, q)

(i) LUMO+7 (l, N)

(j) LUMO+8 (R, r)

(k) LUMO+9 (T, U)
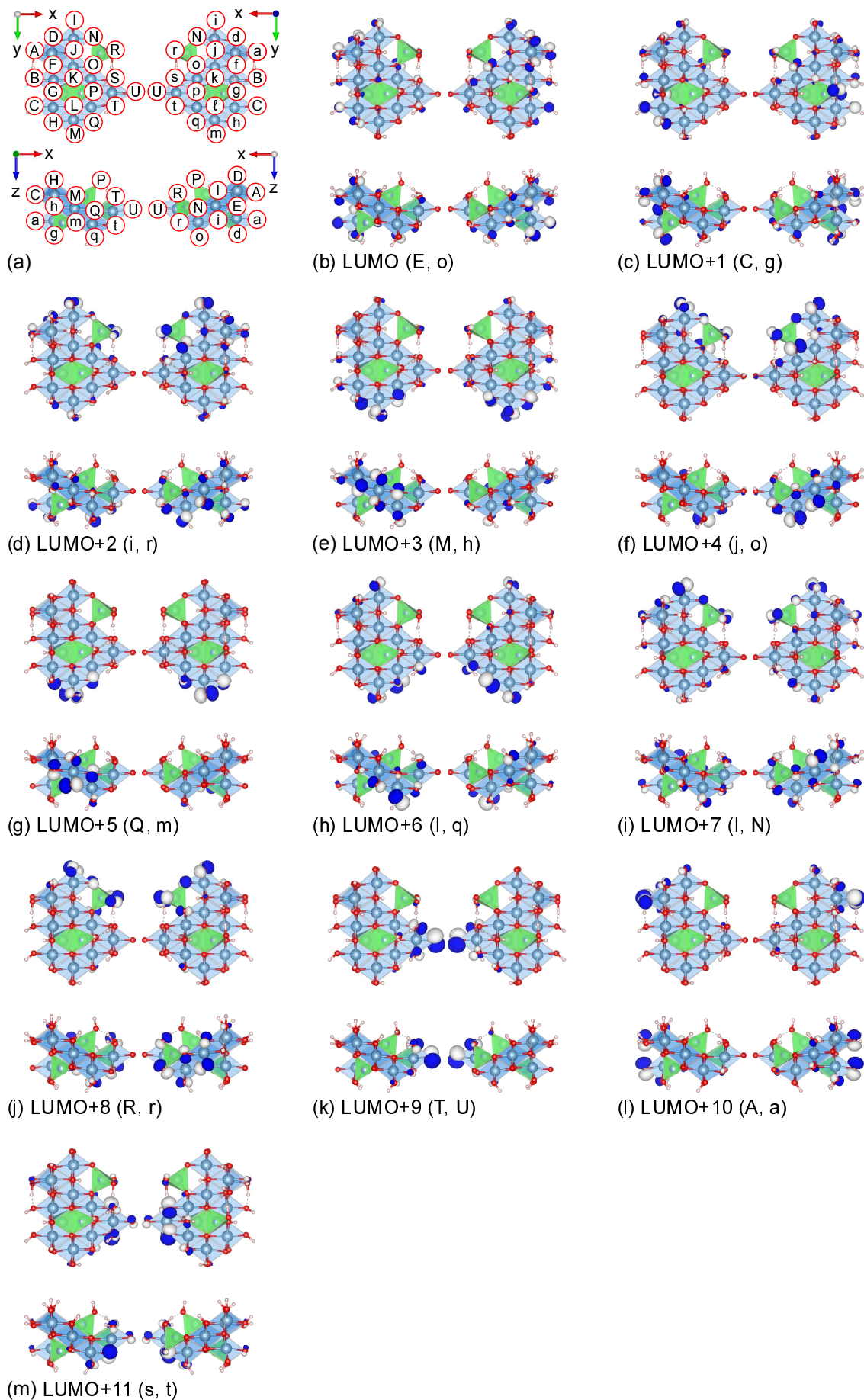
(l) LUMO+10 (A, a)

(m) LUMO+11 (s, t)

Figure S2. (a) Labels of O atoms of the bare cluster. (b)–(m) LUMO–LUMO+11 of the bare cluster. The O atoms that should be terminated by H atoms because of large molecular orbital coefficients are provided in parentheses. Isosurface values are 5.0×10^{-2}. a.u.
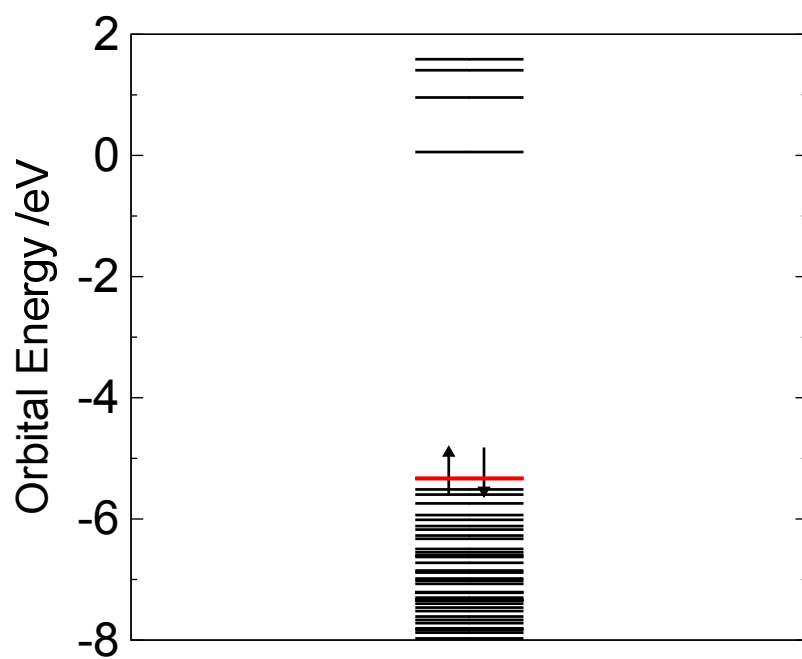
4

Figure S3. Calculated orbital levels of the SSHT cluster model. The energy gap is 5.39 eV.

Table S2. Cartesian coordinates of the SSHT cluster model. The coordinates are provided in Angstrom units.

No.	Atom	x	y	z	No.	Atom	x	y	z
1	Al	-2.5502	3.0942	-0.8695	48	O	5.2249	1.8849	1.2792
2	Al	3.2166	-1.2169	1.6664	49	O	-4.6889	0.8051	2.4615
3	Al	-1.5393	-0.0745	-1.3152	50	O	5.3589	1.2095	-1.4670
4	Al	3.4200	-1.3881	-1.2848	51	O	-5.1650	-1.4838	1.7196
5	Al	-1.0325	-1.1988	1.6144	52	O	-4.4465	0.2456	-0.1377
6	Al	1.7267	3.4648	-0.4740	53	O	-3.2238	4.6504	-1.4638
7	Al	4.1619	1.2338	-0.0048	54	H	-0.3025	3.4943	-2.2320
8	Al	-3.9027	-1.5183	0.3049	55	H	3.3814	-3.7740	-1.2575
9	Al	-3.3571	1.0729	1.1627	56	H	1.6778	-1.5870	-3.1003
10	Al	-0.6281	1.9749	1.0517	57	H	-3.0948	1.4581	-2.7084
11	Al	1.2776	0.2910	0.0178	58	H	-1.2750	-5.7087	-0.6665
12	Al	0.7433	-2.2661	-0.9075	59	H	2.4161	-1.2264	3.8830
13	Al	-1.8693	-3.2133	-0.6837	60	H	-1.2305	2.1810	-2.8075
14	O	-0.4508	-1.7859	3.2118	61	H	1.7527	-3.9919	0.4531
15	O	1.1962	4.0541	-2.0353	62	H	0.8763	-1.6662	3.1542
16	O	4.0528	-3.1077	-0.9378	63	H	4.4182	-3.3290	2.1297
17	O	2.7527	0.7012	1.2228	64	H	2.6147	0.9433	-2.0955
18	O	-1.9346	1.3556	-0.2431	65	H	-0.0233	3.1316	3.2074
19	O	-0.5662	-2.3646	0.3723	66	H	0.1691	-4.6243	-0.3052
20	O	2.8207	0.5138	-1.2330	67	H	-0.7992	-2.6022	3.6363
21	O	-5.0136	-2.4729	-0.9316	68	H	-5.3616	-1.8834	-1.6464
22	O	-2.0283	1.8322	2.3045	69	H	1.7379	5.5453	0.9977
23	O	1.9749	-1.4832	3.0373	70	H	5.2130	-1.4785	-3.0162
24	O	-1.2246	3.0410	-2.2778	71	H	6.1809	1.6539	1.3343
25	O	1.3252	-4.0322	-0.4446	72	H	-4.2572	-3.2741	-1.4077
26	O	-3.7172	2.0835	-2.1075	73	H	-5.4722	1.4035	2.3806
27	O	-0.9863	-4.8499	-0.2816	74	H	-3.3846	-3.8344	1.3581
28	O	4.4445	-0.7267	2.8799	75	H	-0.3270	-3.6149	-2.7614
29	O	-2.6935	-0.6290	1.4533	76	H	5.1581	0.2420	-2.1452
30	O	3.4820	2.9984	-0.3267	77	H	2.4791	1.2776	1.9776
31	O	0.8436	2.0471	-0.0863	78	H	-1.8570	0.0726	-3.7532
32	O	-0.0033	0.2405	1.3385	79	H	4.0737	3.5486	0.2505
33	O	2.1207	-1.4103	0.1288	80	H	4.8517	0.1673	2.7492
34	O	-1.2723	3.6264	0.3936	81	H	-4.5038	0.7685	-0.9782
35	O	-3.8041	2.8138	0.5731	82	H	-5.0325	-0.4170	2.2211
36	O	4.4883	-0.6683	0.1399	83	H	-3.0618	-3.6900	-2.7464
37	O	-3.1081	-3.1683	0.7013	84	H	0.9085	3.7835	1.9153
38	O	-2.5618	-1.4750	-1.0319	85	H	5.5914	2.0413	-1.9385
39	O	0.1992	-0.4509	-1.2645	86	H	1.4333	4.8380	-2.5729
40	O	-1.9214	0.6541	-2.9605	87	H	-1.9424	1.2946	3.1263
41	O	4.6498	-0.8188	-2.5521	88	H	-3.9527	5.0606	-0.9370
42	O	-3.2263	-3.9387	-1.8010	89	H	-4.2246	2.7701	-2.6092
43	O	2.0495	-2.0500	-2.3176	90	H	5.4101	-0.9795	0.2964
44	O	-0.5691	-2.9512	-2.0781	91	H	4.0413	-3.1975	0.2902
45	O	3.7946	-2.9858	1.4495	92	H	-3.6800	3.4878	1.2846
46	O	0.4584	2.9261	2.3711	93	H	-0.8927	4.5192	0.5244
47	O	1.4592	4.6146	0.8687	94	H	-6.1008	-1.6834	1.4785

6

Table S3. OVCCs for the effective mode of the γ-alumina cluster model. The core orbitals are neglected.

i		Energy / eV	$f_{i,\xi} \times 10^{-3}$ a.u.
265	HOMO	-5.921	1.525
263	HOMO-2	-8.861	1.052
264	HOMO-1	-8.978	1.038
260	HOMO-5	-9.161	0.840
$\vdots$	$\vdots$	$\vdots$	$\vdots$
149	HOMO-116	-17.613	0.007
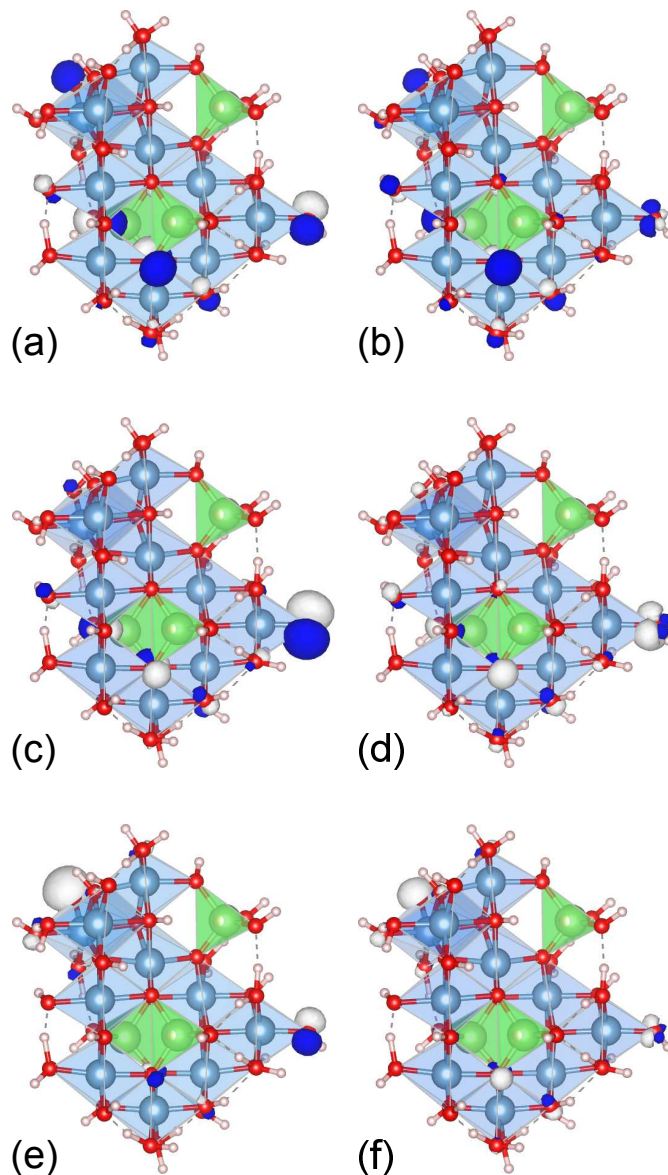
Figure S4. (a) HOMO, (b) OVCD for the HOMO, (c) HOMO-2, (d) OVCD for the HOMO-2, (e) HOMO-1, and (f) OVCD for the HOMO-1 of the γ-alumina cluster model. Isosurface values of the molecular orbitals are 5.0×10^{-2} a.u., and of the OVCDs are 2.0×10^{-5} a.u.
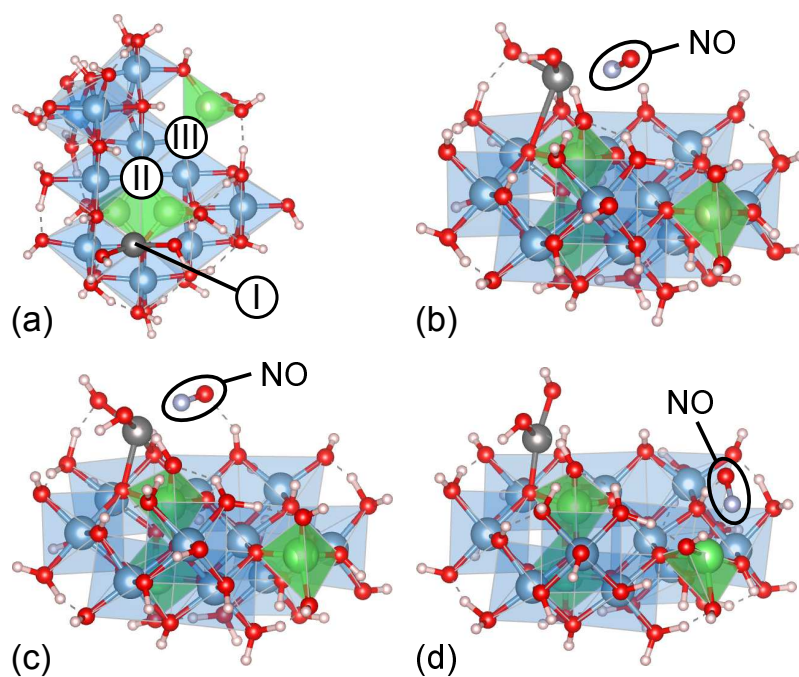
Figure S5. (a) Initial positions of NO on the Cu(OH)$_2$/γ-alumina cluster model. Geometry-optimized structures obtained by initially placing NO on positions (b) I, (c), II, or (d) III. The total energies of (c) and (d) respectively are 0.261 and 1.416 eV higher than that of (b). The reference of the total energy is that of (b), -8068.23720195 a.u.
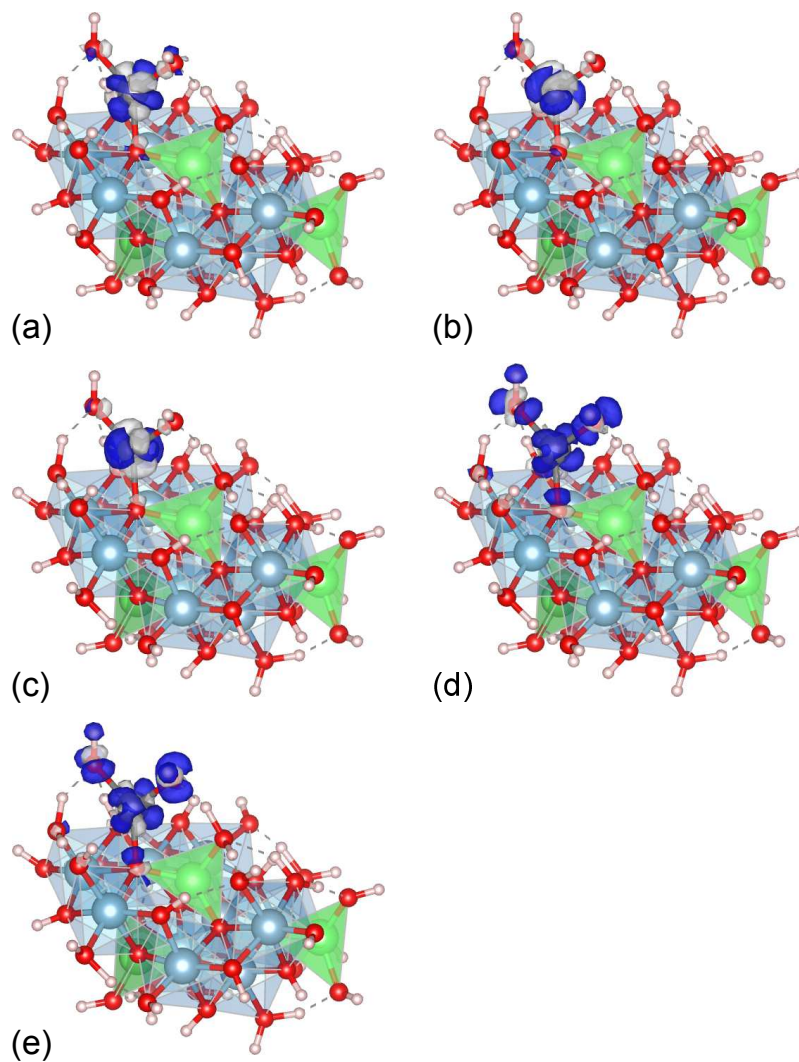
Figure S6. Electron density differences of the Cu(OH)$_2$/γ-alumina cluster model between (a) S$_1$ and S$_0$, (b) S$_2$ and S$_0$, (c) S$_4$ and S$_0$, (d) S$_6$ and S$_0$, and (e) S$_{12}$ and S$_0$. Isosurface values are 5.0×10^{-3} a.u.

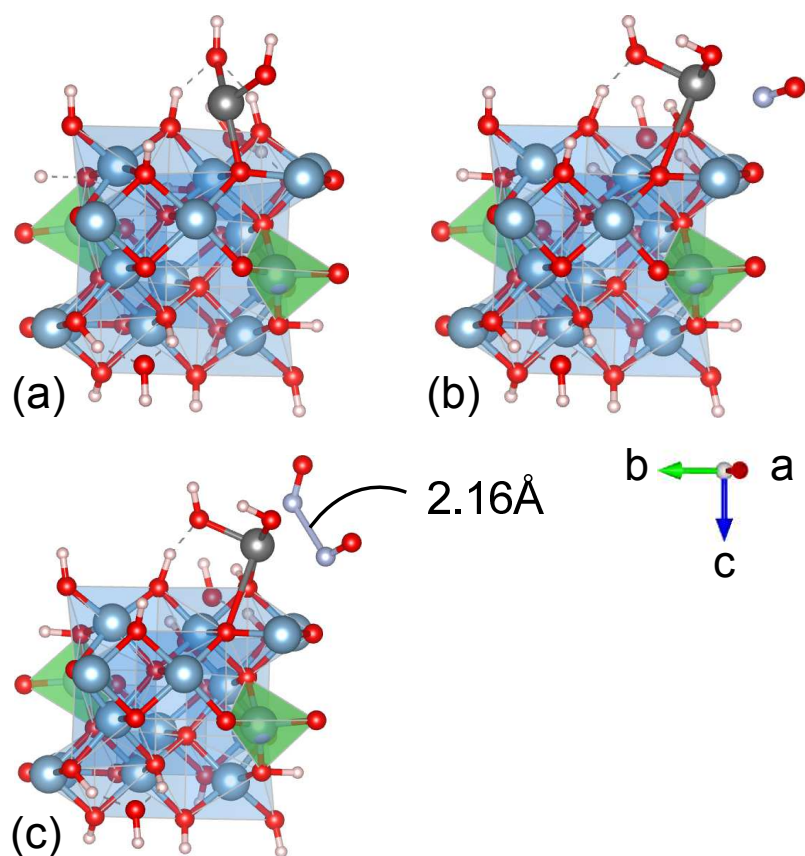Figure S7. Geometry-optimized structures of the (a) $Cu(OH)_2/\gamma$-alumina, (b) NO-adsorbed $Cu(OH)_2/\gamma$-alumina, and (c) $(NO)_2$-adsorbed $Cu(OH)_2/\gamma$-alumina slab models.
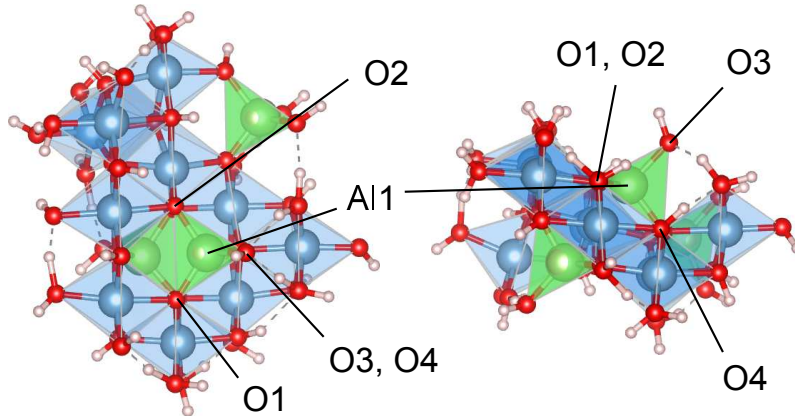
Figure S8. Atomic labels of the tetrahedral Al species on which $Cu(OH)_2$ is adsorbed.

Table S4. Interatomic distance and Mulliken charge of the tetrahedral Al species in Fig. S8 before and after the Cu adsorption.

| | | d (Å) | | | | Mulliken charge | | | | |
		Al1-O1	Al1-O2	Al1-O3	Al1-O4	Al1	O1	O2	O3	O4
Cluster model	γ-alumina	1.757	1.779	1.839	1.830	0.928	-0.876	-0.860	-0.723	-0.920
	Cu/γ-alumina	1.823	1.775	1.819	1.804	1.043	-0.877	-0.864	-0.799	-0.935
Slab model	γ-alumina	1.791	1.772	1.800	1.859	1.311	-1.004	-1.017	-0.931	-1.008
	Cu/γ-alumina	1.845	1.753	1.785	1.837	1.436	-0.898	-1.026	-0.948	-1.018

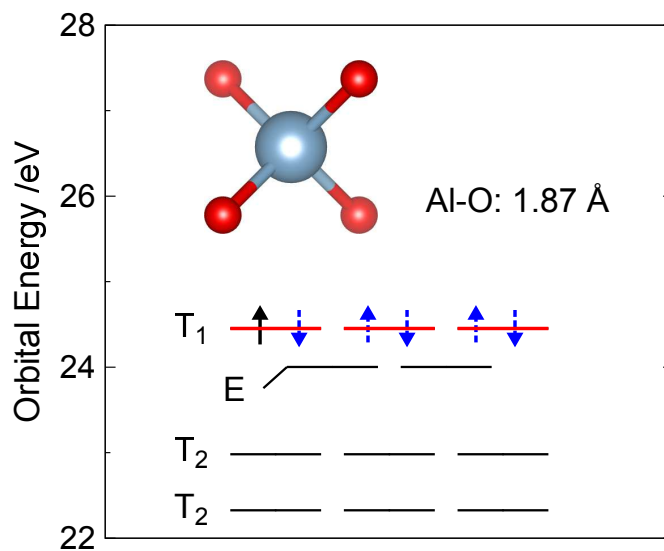Figure S9. Orbital levels of the geometry-optimized AlO$_4$ with the T_d symmetry. Five electrons are provided to obtain the appropriate oxidation number.

Table S5. VCCs of AlO$_4$.

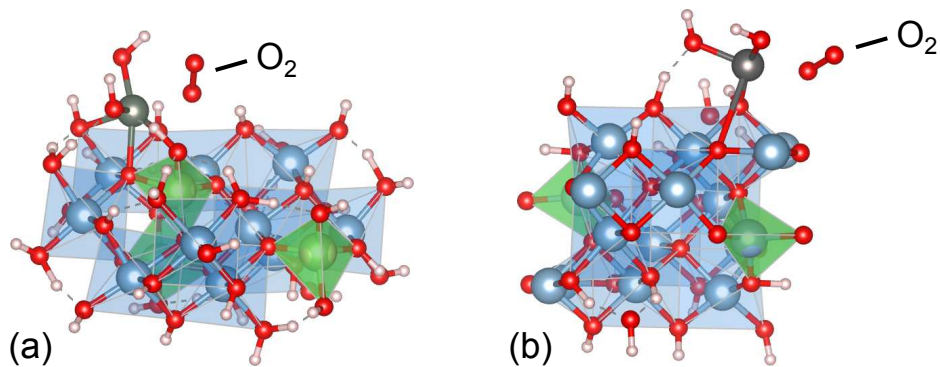|	Frequency (cm^{-1})	VCC (10^{-4} a.u.)
e	267.1	0.0000
t_2	336.0	0.8621
a_1	509.0	2.1265
t_2	582.9	1.1002

Figure S10. Geometry-optimized structures of the O_2-adsorbed $Cu(OH)_2/\gamma$-alumina (a) cluster and (b) slab models.

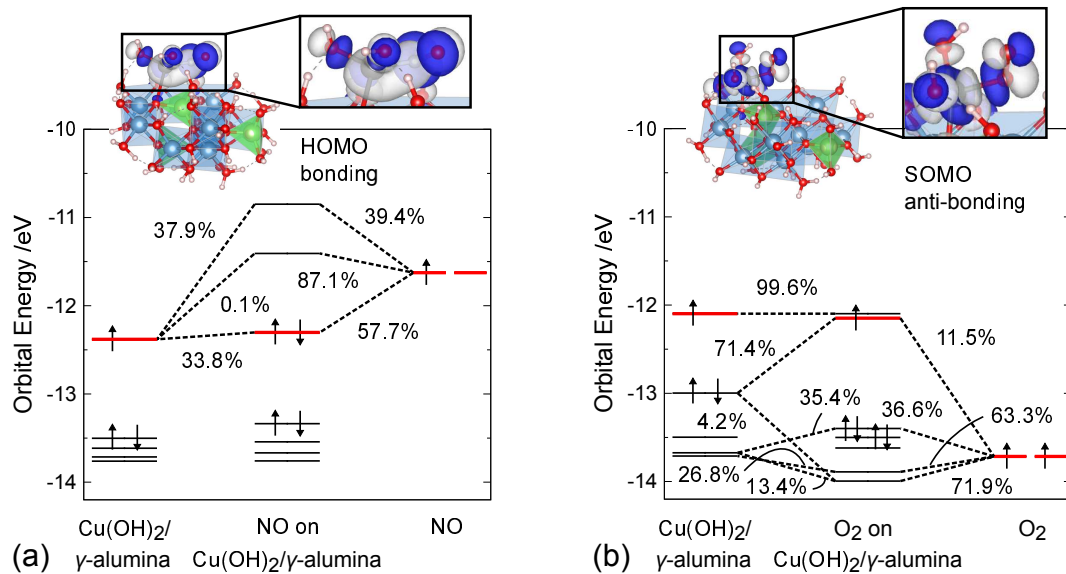Figure S11. Fragment orbital analyses of the (a) NO- and (b) O_2-adsorbed $Cu(OH)_2/\gamma$-alumina cluster models. Values of P_{km} are provided in percentages.